



Failure Behavior of Glass and Aluminum Oxynitride (AlON) Tiles Under Spherical Indenters

by Trevor E. Wilantewicz

ARL-TR-5180

May 2010

NOTICES

Disclaimers

The findings in this report are not to be construed as an official Department of the Army position unless so designated by other authorized documents.

Citation of manufacturer's or trade names does not constitute an official endorsement or approval of the use thereof.

Destroy this report when it is no longer needed. Do not return it to the originator.

Army Research Laboratory

Aberdeen Proving Ground, MD 21005-5066

ARL-TR-5180**May 2010**

Failure Behavior of Glass and Aluminum Oxynitride (AlON) Tiles Under Spherical Indenters

Trevor E. Wilantewicz
ARL/Oak Ridge Associated Universities

REPORT DOCUMENTATION PAGE				Form Approved OMB No. 0704-0188	
Public reporting burden for this collection of information is estimated to average 1 hour per response, including the time for reviewing instructions, searching existing data sources, gathering and maintaining the data needed, and completing and reviewing the collection information. Send comments regarding this burden estimate or any other aspect of this collection of information, including suggestions for reducing the burden, to Department of Defense, Washington Headquarters Services, Directorate for Information Operations and Reports (0704-0188), 1215 Jefferson Davis Highway, Suite 1204, Arlington, VA 22202-4302. Respondents should be aware that notwithstanding any other provision of law, no person shall be subject to any penalty for failing to comply with a collection of information if it does not display a currently valid OMB control number. PLEASE DO NOT RETURN YOUR FORM TO THE ABOVE ADDRESS.					
1. REPORT DATE (DD-MM-YYYY) May 2010		2. REPORT TYPE Final		3. DATES COVERED (From - To) January 2007–January 2008	
4. TITLE AND SUBTITLE Failure Behavior of Glass and Aluminum Oxynitride (AlON) Tiles Under Spherical Indenters				5a. CONTRACT NUMBER	
				5b. GRANT NUMBER	
				5c. PROGRAM ELEMENT NUMBER	
6. AUTHOR(S) Trevor E. Wilantewicz *				5d. PROJECT NUMBER AH 80	
				5e. TASK NUMBER	
				5f. WORK UNIT NUMBER	
7. PERFORMING ORGANIZATION NAME(S) AND ADDRESS(ES) U.S. Army Research Laboratory RDRL-WMT-D Aberdeen Proving Ground, MD 21005-5066				8. PERFORMING ORGANIZATION REPORT NUMBER ARL-TR-5180	
9. SPONSORING/MONITORING AGENCY NAME(S) AND ADDRESS(ES)				10. SPONSOR/MONITOR'S ACRONYM(S)	
				11. SPONSOR/MONITOR'S REPORT NUMBER(S)	
12. DISTRIBUTION/AVAILABILITY STATEMENT Approved for public release; distribution is unlimited.					
13. SUPPLEMENTARY NOTES * ARL/Oak Ridge Associated Universities					
14. ABSTRACT The failure behavior of glass and ceramic tiles during quasi-static loading from spherical indenters is studied. The failure behavior is examined on both a micro- and macro-size scale. The former is achieved by using a small spherical diamond indenter to study the localized contact behavior, and the latter is achieved by loading large tiles to complete structural failure using a unique test configuration. The influence of tile thickness and indenter radius on the failure behavior is also examined. Information on fundamental damage mechanisms in glass and ceramic materials subjected to localized contact, including the onset of inelastic deformation and the initiation of cracks, may be meaningful in relation to screening and ranking brittle materials for failure resistance.					
15. SUBJECT TERMS ceramics, glass, indentation					
16. SECURITY CLASSIFICATION OF:			17. LIMITATION OF ABSTRACT UU	18. NUMBER OF PAGES 68	19a. NAME OF RESPONSIBLE PERSON Trevor E. Wilantewicz
a. REPORT Unclassified	b. ABSTRACT Unclassified	c. THIS PAGE Unclassified			19b. TELEPHONE NUMBER (Include area code) 410-306-0711

Contents

List of Figures	v
List of Tables	viii
1. Introduction	1
1.1 Multiaxial Dynamic Failure Modes in Ceramics and Glasses	1
1.2 Objectives	1
2. Background Review	2
2.1 Hertzian Contact.....	2
2.2 Cracking Behavior (Elastic Contact).....	3
2.3 Cracking Behavior (Elastic-Plastic Contact).....	3
2.4 Multiaxial Failure	4
3. Material Selection	5
3.1 Glass Materials	5
3.2 Ceramic Materials	5
4. Experimental Procedures, Results, and Discussion	6
4.1 Instrumented Indentation Testing (IIT).....	6
4.1.1 IIT Equipment	6
4.1.2 Yield Stress Measurements	10
4.1.3 Indentation Damage Patterns.....	14
4.1.4 IIT Load-Displacement Data Analysis.....	25
4.1.5 In-Situ Crack Initiation Observation	28
4.2 Structural Failure Experiments.....	34
4.2.1 Tile Preparation and Testing	35
4.2.2 Failure Test Results	37
4.2.3 Flaw Size Estimates.....	47
4.3 Other Experiments.....	47
5. Summary and Conclusions	49

6. Future Work	50
7. References	51
Appendix. Hertzian Equations	55
Distribution List	57

List of Figures

Figure 1. Schematic of Hertzian contact loading. Idealized cross section showing the ring-cone crack system and several measurable features.	2
Figure 2. Schematic of Zwick hardness measuring head. Key components are shown.	7
Figure 3. Schematic of a test sequence illustrating how the load and displacement data are collected. Also shown are the speeds (V) corresponding to the different steps involved for a test.....	7
Figure 4. Load-displacement traces in polycrystalline aluminum from Vickers indentation.....	9
Figure 5. Vickers indentation in polycrystalline aluminum made at 20-N load.....	9
Figure 6. Residual indentation depth as a function of load for the three glass materials using a spherical 500- μm -diameter single-crystal diamond indenter. Tin side of the Starphire and Borofloat glasses was tested.....	10
Figure 7. Straight line fits through high-load data points for determining load at “full” plastic yield. The x-intercept marks this load. Error bars are same as in figure 6.	12
Figure 8. Residual indentation depth as a function of load for AlON using a spherical 500- μm -diameter single-crystal diamond indenter.....	13
Figure 9. Straight line fit through high-load data points in AlON for determining load at “full” plastic yield.	13
Figure 10. Indentation sites in the tin side of Starphire glass produced with spherical 500- μm -diameter single-crystal diamond indenter.....	15
Figure 11. Load-displacement traces for the tin side of Starphire glass. The curves correspond to the same indentation sites shown in figure 10. Curves produced with spherical 500- μm -diameter single-crystal diamond indenter.	16
Figure 12. The 200-N indentation site in tin side of Starphire glass and corresponding load-displacement trace for test showing catastrophic failure under indenter. The 500- μm -diameter spherical diamond indenter used.....	17
Figure 13. Indentation sites in the tin side of Borofloat glass produced with spherical 500- μm -diameter single-crystal diamond indenter.....	19
Figure 14. Load-displacement traces for the tin side of Borofloat glass. The curves correspond to the same indentation sites shown in figure 13. Curves produced with spherical 500- μm -diameter single-crystal diamond indenter.	20
Figure 15. Indentation sites in silica glass produced with spherical 500- μm -diameter single-crystal diamond indenter.....	21
Figure 16. Load-displacement traces for the silica glass. The curves correspond to the same indentation sites shown in figure 15. Curves produced with spherical 500- μm -diameter single-crystal diamond indenter.....	22
Figure 17. Indentation sites in polycrystalline AlON produced with spherical 500- μm -diameter single-crystal diamond indenter.....	23

Figure 18. Load-displacement traces for AlON. The curves correspond to the same indentation sites shown in figure 17. Curves produced with spherical 500- μm -diameter single-crystal diamond indenter.	24
Figure 19. An example of deformation twinning inside a 150-N indentation in AlON produced with 500- μm -diameter spherical diamond indenter.	25
Figure 20. Elastic recovery and percent elastic recovery as a function of the maximum indentation load for glass and AlON materials. Data for tin sides are plotted for Starphire and Borofloat glasses.	26
Figure 21. Comparison of elastic recovery behavior of tin and air sides of Starphire glass.	26
Figure 22. Maximum penetration depth as a function of load for the three glass materials and AlON.	27
Figure 23. Experimental setup for observing the crack initiation behavior of transparent materials in real time with the IIT system.	28
Figure 24. In-situ indentation patterns in the tin sides of Starphire (left) and Borofloat (right) glasses: (a) $F < F_c$, (b) $F = F_c$, (c) $F = F_{\text{max}} = 150 \text{ N}$, and (d) complete unloading ($F = 0 \text{ N}$) ([a–c] loading cycle and [d] unloading cycle).	31
Figure 25. In-situ indentation patterns in silica glass (left) and AlON (right): (a) $F < F_c$, (b) $F = F_c$, (c) $F = F_{\text{max}}$, and (d) complete unloading ($F = 0 \text{ N}$) ([a–c] loading cycle and [d] unloading cycle).	32
Figure 26. The 150-N indentation sites in Starphire glass for both air and tin sides made with 500- μm -diameter spherical diamond indenter.	34
Figure 27. Picture of the experimental setup used to study the structural failure behavior of the tiles.	35
Figure 28. Starphire tile both as-received and after 220-grit abrasion: (a) as-received air side, (b) after abrasion air side, (c) as-received tin side, and (d) after abrasion tin side. All images 250 \times original magnification.	36
Figure 29. Failure load for the 3.2-mm-thick Starphire glass tiles loaded with steel balls of different diameter.	39
Figure 30. Failure load for the 6-mm-thick Starphire glass tiles loaded with steel balls of different diameter.	39
Figure 31. Failure load for 12-mm-thick Starphire glass tiles loaded with steel balls of different diameter.	40
Figure 32. Several failed 3.2-mm Starphire tiles. The star-like fracture patterns are typical of biaxial flexural testing. Top row, left to right: 0.125-, 0.25-, and 0.5-in ball. Bottom row, left to right: 0.5-in ball and only bottom surface abraded, 0.0625-in ball. Tiles are 4 \times 4 in ²	41
Figure 33. As-received 3.2-mm Starphire tile loaded to failure with 0.5-in steel ball. Tile is 4 \times 4 in ²	41
Figure 34. Mean contact stress at the initiation load for ring-cone cracks as a function of the ball diameter for the tin side of Starphire glass. Data for an unabraded tile.	42

Figure 35. Failed 6-mm Starphire tiles that formed no macro conoid (a) and that did form a macro conoid (b). Tension side faces up (a) and compression side faces up (b). Steel ball diameter 0.0625 in. Tiles are $4 \times 4 \text{ in}^2$	44
Figure 36. Failed 12-mm Starphire tile loaded with a 0.75-in-diameter steel ball. The tension side, illustrating the large crater formed from the macro conoid, faces up. The chipped away pieces are not shown.	44
Figure 37. A sequence of frames illustrating the formation and growth of the ring-cone crack (a–c), and the initiation of the spall failure (d) in the 12-mm Starphire tile (tin side) contacted with the 0.25-in-diameter steel ball. Load increases from a to d.....	46
Figure 38. Average failure load as a function of tile thickness. Two different curve fits of the data show the exponential or power-law dependence on tile thickness.....	46
Figure 39. Ring crack stress as a function of ball diameter for the tin sides of unabraded Starphire and Borofloat glasses.	47
Figure 40. Ring crack load as a function of ball diameter for the tin sides of unabraded Starphire and Borofloat glasses.	48

List of Tables

Table 1. Material mechanical data.	5
Table 2. IIT accuracy test results.	9
Table 3. Residual depth.....	11
Table 4. Yield data.	12
Table 5. Deformation and fracture loads.	14
Table 6. Crack initiation summary.....	29
Table 7. Acoustic emission data.	33
Table 8. Starphire glass failure test results.	38

1. Introduction

1.1 Multiaxial Dynamic Failure Modes in Ceramics and Glasses

The failure of ceramic and glass materials under ballistic loading is a complex process involving a number of distinct multiaxial dynamic failure modes (1–5). These failure modes include, but are not limited to, (1) front- and back-face radial cracking, (2) pulverization (comminution) in the vicinity of the penetrator, (3) microcracking, (4) steep and shallow cone cracking, and (5) lateral cracking.

These failure modes are not particular to just ballistic impacts, since they are also observed to varying extents in dynamic impacts of spheres and rods on ceramics (1, 6–14) and glass (8, 15–17) at less than ballistic velocities, and even in quasi-static spherical (Hertzian) and cylindrical punch indentation tests (18–26). The formation of very narrow shear bands under impact sites in boron carbide has been observed as well and is thought to be the result of localized shear failure of the material (12).

The fact that many of the failure modes seen in ballistic impact tests can be reproduced under quasi-static loading conditions under an indenter provides some motivation for the current work.

Although it is recognized that actual ballistic testing is the definitive way to judge material and system performance, it is usually time consuming and costly to conduct, and not possible on prototype or experimental materials that may be too small or in limited supply.

Much effort has been devoted to understanding the material properties that govern ballistic performance (27–32) in order to guide research and development of new materials that perform better, while still being lightweight and cost-effective to produce. However, one challenge that still exists is to create a simple set of experiments that may be used to successfully screen and down-rank candidate armor materials in terms of intrinsic (material) performance potential. The current work may possibly form part of such a screening test.

1.2 Objectives

The failure behavior of glass and ceramic tiles to quasi-static loading from spherical indenters forms the basis of the current study. The failure behavior is examined on both a micro- and macro-size scale. The former is achieved by using a small spherical diamond indenter to study the localized contact behavior, and the second is achieved by loading large tiles to complete structural failure using a unique test configuration.

The influence of tile thickness and indenter radius on the failure behavior is also examined. By varying the tile thickness and indenter radius, researchers hope to achieve different failure behavior, which might be meaningful in helping to screen candidate materials. Information on

fundamental damage mechanisms in glass and ceramic materials subjected to localized contact, including the onset of inelastic deformation and the initiation of cracks, may possibly be meaningful in relation to screening and ranking materials for potential ballistic protection design.

2. Background Review

2.1 Hertzian Contact

The contact of an elastic sphere on a rigid elastic body is referred to as Hertzian contact, named after Heinrich Rudolf Hertz (33), who first studied this contact situation. A schematic of this contact condition is shown in figure 1. If the contact remains entirely frictionless and elastic, then the Hertz equations relating the contact load, contact radius, and stress are valid. With either the onset of fracture or plasticity, or the presence of friction, the equations are no longer strictly valid (22).

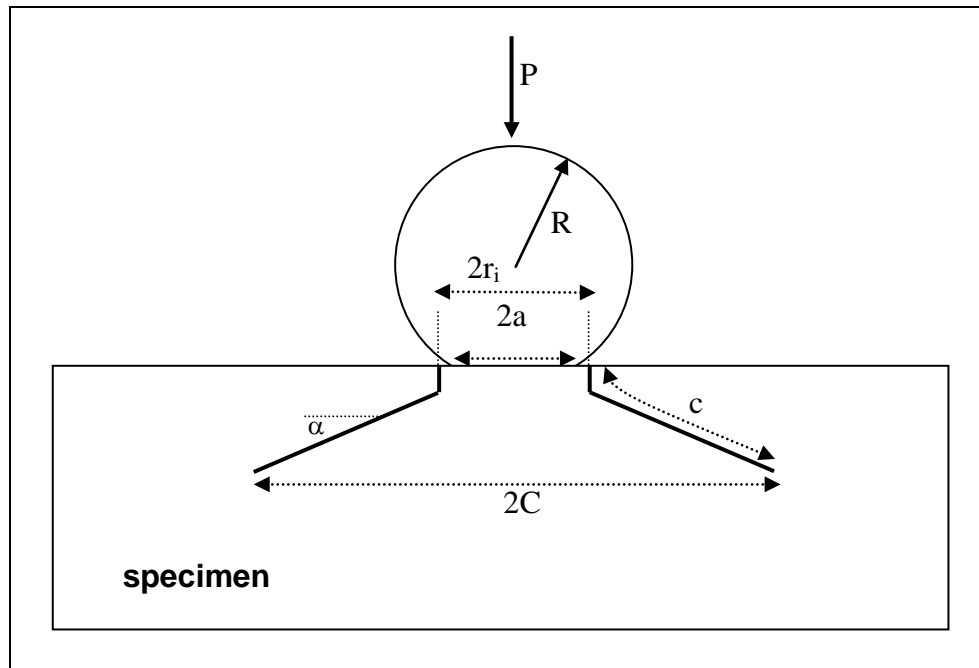


Figure 1. Schematic of Hertzian contact loading. Idealized cross section showing the ring-cone crack system and several measurable features.

However, it is for these reasons the test is used, i.e., to study the deformation and fracture response of materials to localized contact. Of the two responses, the onset of plasticity invalidates the use of the Hertz equations more than fracture does, since the latter can be nearly

reversible (elastic) under certain conditions. In addition, one is usually concerned with the stress level just up to the point of fracture, or yield, where the Hertz equations are valid.

Indentation contacts can be characterized as either “sharp” or “blunt” depending on whether inelastic or elastic deformation of the specimen precedes fracture, respectively (22). Thus, the ball indenter radius can be chosen so as to either promote or prevent yield before fracture. For Hertzian fracture tests, the ball radius is usually chosen to be large enough to promote fracture before yield. However, yielding may occur after fracture if the loads are further increased, since the mean contact stress continues to increase with load.

The indenter material is usually chosen such that its elastic and strength properties considerably overmatch the specimen to be examined, e.g., steel or tungsten carbide balls for glass specimens and tungsten carbide or diamond balls for ceramic specimens. This ensures that the majority of deformation and fracture occurs in the specimen and not the indenter. The appendix defines the pertinent Hertzian equations used in this study.

2.2 Cracking Behavior (Elastic Contact)

Generally speaking, one of two scenarios with respect to ring and cone crack initiation can occur when a ball indenter is loaded onto the surface of a rigid brittle material. The following results are primarily based on observations in glass because of its transparency: (1) unstable initiation (“pop-in”) of the entire ring-cone crack system or (2) initiation of the ring crack, stable growth of the ring crack downward, followed by unstable initiation of the cone crack.

In both scenarios, after the unstable initiation of the cone crack, the crack grows stably with further increase of the load. That is, the strain energy release rate decreases as the crack extends, thus making the Hertzian cone a stable crack system. This is to be expected, since the base of the cone crack grows larger with increasing load, thus supporting the load. More detailed discussions of the initiation behavior can be found elsewhere in several good references (22, 23, 34–46).

On unloading, the cone crack is usually observed to retract some, and then at a critical load a portion of the cone surface usually detaches itself from the rest. This can generate an intense acoustic emission signal. Because of this, the cone crack is highly visible under load, but after load removal its visibility decreases, except for the portion close to the surface.

2.3 Cracking Behavior (Elastic-Plastic Contact)

If the ball indenter has a sufficiently small diameter, or if a sufficiently high contact load is achieved, the material may transition from elastic to elastic-plastic during the course of loading. For glasses, the term plastic is being used loosely to indicate inelastic deformation has ensued.

For example, Swain and Hagan (47) observed plastic yielding and the formation of ring-cone, radial, and lateral cracks in soda-lime-silica glass indented with 0.49- and 1.0-mm-diameter spherical tungsten carbide indenters and 1.0-mm-diameter spherical diamond indenters. On

loading, elastic deformation took place first, followed by the formation of surface ring cracks, and then subsurface plasticity. Occasionally a large cone crack would initiate from the surface ring crack, but this usually did not occur. Continued loading produced subsurface median cracks.

On unloading, the median cracks were observed to start closing, and subsequently, radial cracks initiated. The radial cracks were sometimes extensions of the median cracks, but in most cases they were observed to initiate separately at the edge of the contact impression. Lateral cracks, whose orientation are mainly parallel to the surface, were observed to initiate just prior to complete load removal.

Hagan and Swain (48) show evidence that the initiation of median cracks about Vickers and small-diameter sphere indentations in soda-lime-silica glass are the result of intersections of shear flow lines beneath the surface that occur at high loads, while smaller radial cracks were found to extend from the corners of the indentations at the surface for smaller loads. The shear flow lines constituted a subsurface region of damage (damage zone) directly below the indentation. Subsurface lateral cracks were also observed and found to be extensions of the shear faults.

Lawn et al. (49) show strong evidence that radial cracks in soda-lime-silica glass can also be the result of extensions of shear flow lines at the surface. Harano et al. (50) have examined the initiation of cracks in chemically strengthened (ion-exchanged) glasses with a Vickers indenter and found that median and radial cracks did not initiate despite the fact the damage zones beneath the indents were deeper than the surface compressive stress layers. They interpreted this to mean that radial and median cracks must also form near the surface, since radial and median cracks formed in the unstrengthened specimens for the same load. Thus, it appears there is still some uncertainty regarding the location of median crack initiation in glass.

2.4 Multiaxial Failure

Lardner et al. (51) examined the fracture of glass plates of varying thickness (1, 1.83, and 3 mm) supported by 3-mm-thick substrates of glass, steel, and poly(methyl methacrylate) (PMMA) using a 12.7-mm-diameter WC-6% Co spherical indenter. Depending on the glass thickness and substrate material, different fracture behaviors were observed.

Lardner et al. found that the fracture patterns fell into four categories: (1) ring, cone, and back-face radial cracking, (2) ring cracking and back-face radial cracking, (3) back-face radial cracking, and (4) ring and cone cracking. The last mode was seen for the 3-mm-thick glass samples regardless of the substrate material. Back-face radial cracking occurred for the 1-mm-thick samples, which were supported by steel, indicating that localized bending of the specimens can still take place even with rigid support.

Part of the intent of the current work is to produce a similar variety of failure modes, but with thicker specimens that may be more relevant to ballistic protection design.

3. Material Selection

The materials used in this study were transparent, with the exception of the AlON, which was not as transparent compared to the glasses. This allowed direct observation of the formation of cracks from indentation contact.

3.1 Glass Materials

All glass materials examined in the current work were from commercial glass manufacturers. The glasses were soda-lime-silica float glass (Starphire^{*}), borosilicate float glass (BOROFLOAT[†]), and vitreous silica. The Starphire and Borofloat materials are produced by PPG Industries and Schott Glass, respectively. The vitreous silica specimens were made by Corning Inc.

All glass materials were furnished in the form of 4- × 4-in square tiles with different thickness. The Borofloat tiles were 19 mm thick, while the Starphire tiles were provided in thicknesses of 3.2, 6, and 12 mm with beveled edges. The vitreous silica specimens were provided in thicknesses of 6.35, 19.05, and 25.4 mm. Table 1 lists several mechanical properties of the glasses as provided by the manufacturers.

Table 1. Material mechanical data.

Material	Young's Modulus, E (GPa)	Poisson's Ratio ν	Knoop Hardness (GPa)	Density (g/cm ³)
Starphire	73.1	0.22	4.6 (500 gf)	2.51
Borofloat	63	0.20	4.7 (100 gf)	2.23
Silica glass	72.7	0.16	5.1 (100 gf)	2.201
AlON	323	0.24	18.1 (200 gf)	3.69
Diamond (indenter)	1141	0.07	~70	3.52
Steel (indenter)	200	0.30	~7	7.5

3.2 Ceramic Materials

The ceramic material chosen for study was polycrystalline aluminum oxynitride (AlON). AlON is a transparent ceramic with the spinel crystal structure and has a large, average grain size, i.e., about 150 μm (52). The oxygen and nitrogen anions form a close-packed, face-centered cubic lattice (53, 54).

^{*}Starphire is a registered trademark of PPG Industries.

[†]BOROFLOAT is a registered trademark of Schott Glass.

The approximate composition is $\text{Al}_{23}\text{O}_{27}\text{N}_5$. The cubic structure leads to mainly isotropic behavior; however, the large grain size can introduce anisotropies on a localized scale. For example, microhardness measurements performed on AlON may only sample a single grain depending on the indentation load and hence are susceptible to crystallographic effects.

4. Experimental Procedures, Results, and Discussion

4.1 Instrumented Indentation Testing (IIT)

Instrumented indentation testing (IIT) was utilized to study the deformation and fracture behavior of the materials to localized indentation contact. In this test format, the load and displacement of the indenter into the material are simultaneously, and continuously, monitored throughout the load-unload cycle.

This format provides valuable information on material behavior, including penetration depths, hardness under load, elastic recovery, and energy dissipation that cannot otherwise be obtained from conventional hardness testing equipment.

A 500- μm -diameter spherical diamond indenter was used. It was made from a single crystal by Gilmore Diamond Tools, Inc., (Attleboro, MA) by a special process called precision spindle method. This resulted in a surface that was exceptionally smooth and uniform in diameter.

Temperature and relative humidity were monitored and varied from 22 to 24 °C, and 41% to 58%, throughout the course of all testing, respectively.

4.1.1 IIT Equipment

The IIT equipment consisted of a specialized hardness testing head made by Zwick, Inc., attached to a standard universal testing machine (Model Z005), also made by Zwick. A schematic of the hardness head is shown in figure 2.

The hardness head is attached to a cross member (not shown), which is attached to the test frame (not shown), which provides the up and down linear motion via a stepping motor. A load cell inside the head measured the force, while a transducer measured the displacement to a resolution of 0.02 μm . The load cell had a 2500-N useable range.

The entire system was computer controlled. The test software allowed total user control of the entire indentation process, including loading rate on both loading and unloading, maximum load, hold time at maximum load, type of control (i.e., load or position control), etc. In addition, a variety of results could be reported, including the maximum load, maximum displacement depth, residual indentation depth, hardness under maximum load, total test time, etc. The load and displacement data could be exported for subsequent user analysis as well.

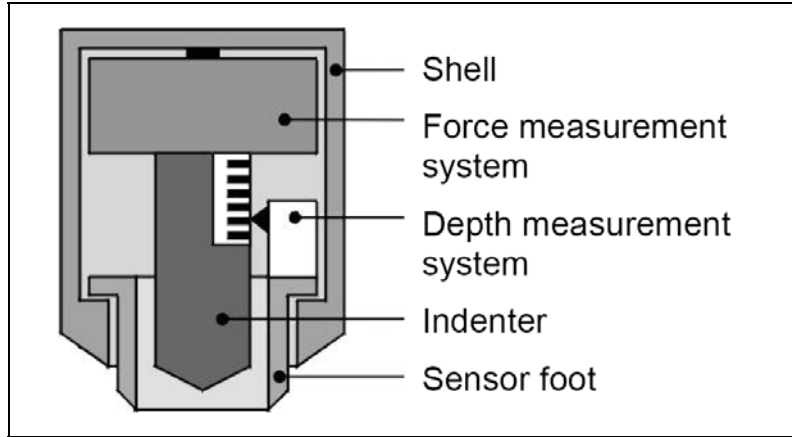


Figure 2. Schematic of Zwick hardness measuring head. Key components are shown.

A schematic illustrating the principles of operation is shown in figure 3. At position 1, the head is sitting above the sample and moves down toward the sample at speed V_{LE} . At step 2, the unit has moved down until the sensor foot contacts the specimen. Further motion downward at speed $V_{pre-test}$ causes the indenter tip to contact the specimen (step 3). However, just before this contact occurs, the speed switches to $V_{contact}$.

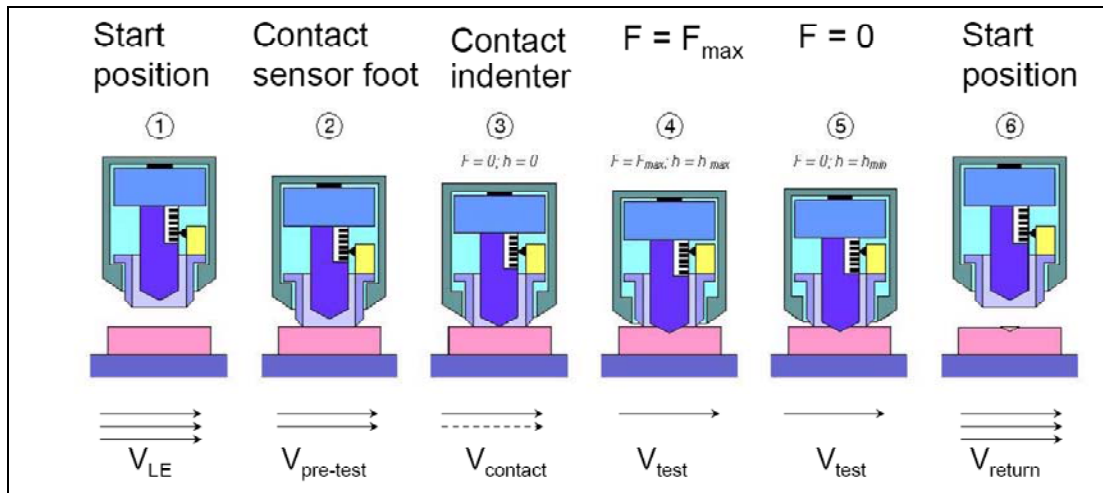


Figure 3. Schematic of a test sequence illustrating how the load and displacement data are collected. Also shown are the speeds (V) corresponding to the different steps involved for a test.

The very slight increase in load brought about by the contact establishes the zero point of the measurement. The speed at which the indenter approaches the sample during this step ($V_{contact}$) is set very low such that the zero point is established very accurately, i.e., with minimal overshoot. Once the zero point is established, the test cycle commences at step 4, in which the displacement rate is set by the user as V_{test} .

For spherical indenters a “preload” can be employed at the beginning of step 4, in which a small load is applied to “settle” the indenter and specimen for the ensuing major test cycle. The preload function does not need to be used but is recommended by the manufacturer. Once the desired maximum load, or displacement, is reached, the indenter is withdrawn at V_{test} (step 5), which can be set different than V_{test} on loading.

At the end of step 5, the load is zero, and if permanent deformation of the sample has occurred, a residual depth of h_{min} is measured. After step 5, the entire hardness head is withdrawn at a rate of V_{return} . Note that the permanent indentation depth is given by the difference in displacement readings of steps 3 and 5, while the maximum displacement depth is given by the difference in readings between steps 3 and 4. The elastic recovery is given by the difference in readings between steps 4 and 5.

Instrument compliance can be a significant factor leading to inaccurate displacement depths, where elastic deformations of the machine are superimposed on those from the specimen. Note that instrument compliance does not affect the value of h_{min} , since all elastic deformations of the machine and specimen are recovered when the load reaches zero, neglecting any anelastic deformations. However, at all other points of the load-displacement curve, the measured depths will not necessarily reflect the actual displacement into the sample due to machine compliance.

Because of the design of the Zwick instrument, the only compliance that is sampled occurs in the indenter material located between the sensor foot and the measurement transducer, which is relatively small. To account for this, the manufacturer has calculated this compliance and factored it out of the displacement readings. The result of this is a displacement measurement that accurately reflects only the inelastic and elastic deformations occurring in the sample.

The compliance factor, as given by the manufacturer, is $0.0049679 \mu\text{m}/\text{N}$. According to the manufacturer, the resolution of the displacement measuring system was $0.02 \mu\text{m}$.

To test the accuracy of the measurement system, a piece of polycrystalline aluminum metal was indented with a Vickers diamond six times at a 20-N load. The diagonals of the resulting indentations were measured under an optical microscope equipped with a digital camera and measurement software.

The depth under load was then calculated for each indentation by dividing the average diagonal length by seven. This stems from the geometry of the Vickers diamond, where the indentation depth is one-seventh the length of the diagonals (49). Since aluminum metal is soft and does not undergo significant elastic recovery, particularly along the diagonals where the plastic strain is very intense, the measurement of the diagonals of the residual indent can give a good measure of the depth under load.

This calculated depth was then compared with the actual depth measured by the IIT. The results are shown in table 2. As shown in table 2, the measured depth was about 8 % lower than the calculated depth, which amounted to an absolute difference of just 2.2 μm . This data is taken as evidence that the IIT gives accurate displacement readings. The load-displacement traces for these tests are shown in figure 4. An indentation in the aluminum is shown in figure 5.

Table 2. IIT accuracy test results.^a

Diagonal Length (μm)	Calculated Depth (μm)	Measured Depth (μm)	Difference (%)
188.3 ± 1.5	26.9 ± 0.2	24.7 ± 0.3	8.0 ± 1.5

^aValues in table are average ± 1 standard deviation

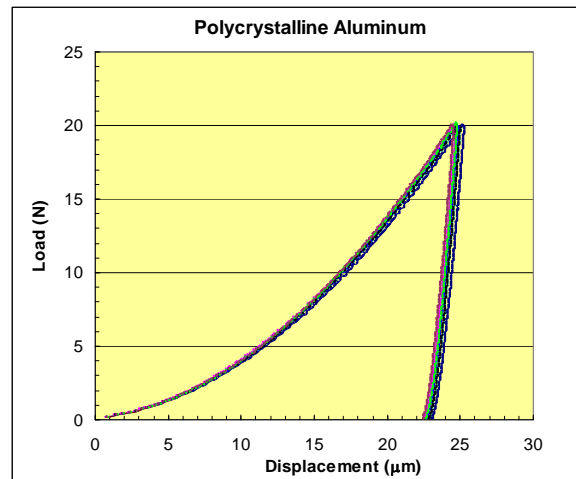


Figure 4. Load-displacement traces in polycrystalline aluminum from Vickers indentation.

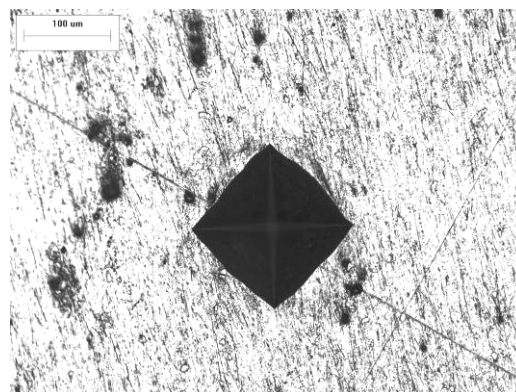


Figure 5. Vickers indentation in polycrystalline aluminum made at 20-N load.

4.1.2 Yield Stress Measurements

The 500- μm -diameter spherical diamond indenter was used to measure the yield stress of the three glass materials and the AION by making indentations at progressively higher loads, starting at 2 N up to 200 N. Ten indentations at each load were made. The “tin” and “air” sides of the Starphire, and the tin side of the Borofloat glasses, were tested.

By plotting the average residual indentation depth as a function of load, the onset of inelastic deformation can be determined. This method is believed to be more sensitive than trying to visually observe when a permanent impression is left in the material, since the deformations may be smaller than the wavelength of light and thus impossible to detect.

According to the manufacturer, the displacement measuring system has a resolution of 0.02 μm , so in principle, it should be able to detect yielding before optical detection can. The results are plotted in figure 6 for the three glass materials. At low loads the materials behave elastic, but as the load is increased a permanent set depth begins to appear. Table 3 lists the residual depths as a function of load. Differences of residual depth between the materials are more noticeable at the higher loads.

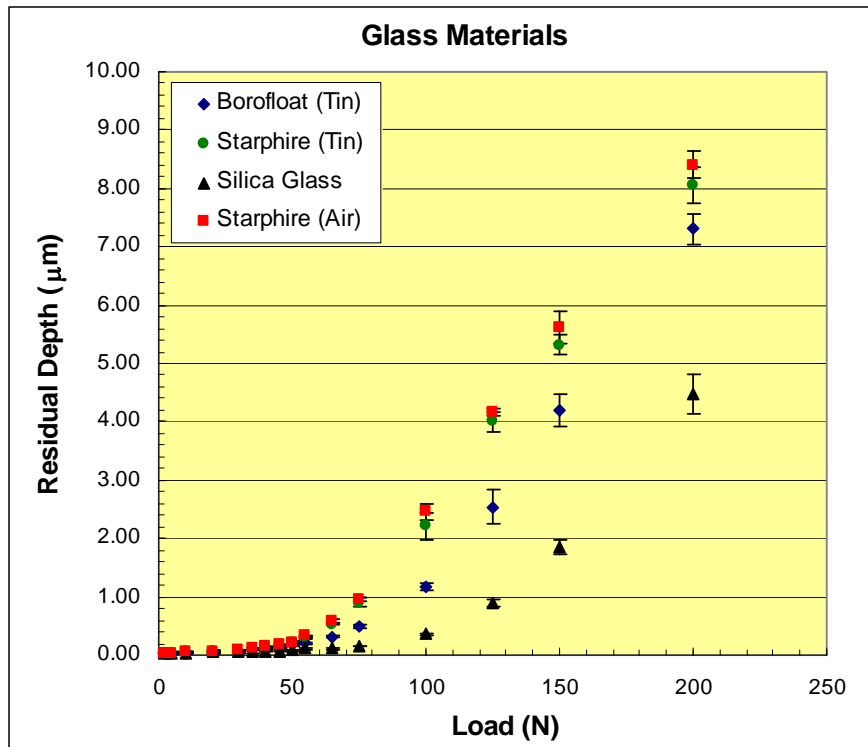


Figure 6. Residual indentation depth as a function of load for the three glass materials using a spherical 500- μm -diameter single-crystal diamond indenter. Tin side of the Starphire and Borofloat glasses was tested.

Table 3. Residual depth.^a

Residual Depth (μm)					
Load (N)	Starphire (Tin)	Starphire (Air)	Borofloat (Tin)	Silica Glass	AION
2	0.03 \pm 0.01	0.03 \pm 0.01	0.04 \pm 0.01	0.03 \pm 0.01	0.02 \pm 0.00
5	0.03 \pm 0.01	0.04 \pm 0.01	0.04 \pm 0.01	0.03 \pm 0.01	0.02 \pm 0.01
10	0.04 \pm 0.02	0.05 \pm 0.01	0.04 \pm 0.01	0.04 \pm 0.01	0.03 \pm 0.01
20	0.05 \pm 0.01	0.07 \pm 0.01	0.05 \pm 0.01	0.05 \pm 0.01	0.04 \pm 0.01
30	0.07 \pm 0.01	0.10 \pm 0.00	0.07 \pm 0.01	0.06 \pm 0.02	0.08 \pm 0.05
35	0.10 \pm 0.02	0.11 \pm 0.01	0.09 \pm 0.01	0.06 \pm 0.02	0.07 \pm 0.05
40	0.11 \pm 0.01	0.14 \pm 0.01	0.11 \pm 0.02	0.07 \pm 0.02	0.12 \pm 0.11
45	0.15 \pm 0.01	0.18 \pm 0.01	0.13 \pm 0.01	0.07 \pm 0.01	0.26 \pm 0.14
50	0.22 \pm 0.02	0.23 \pm 0.01	0.17 \pm 0.01	0.08 \pm 0.02	0.33 \pm 0.18
55	0.30 \pm 0.01	0.33 \pm 0.02	0.21 \pm 0.02	0.11 \pm 0.02	0.32 \pm 0.21
65	0.54 \pm 0.02	0.59 \pm 0.03	0.32 \pm 0.02	0.11 \pm 0.02	0.51 \pm 0.19
75	0.91 \pm 0.09	0.96 \pm 0.04	0.48 \pm 0.03	0.15 \pm 0.01	0.72 \pm 0.10
100	2.21 \pm 0.24	2.46 \pm 0.14	1.16 \pm 0.06	0.36 \pm 0.02	1.12 \pm 0.16
125	4.00 \pm 0.16	4.18 \pm 0.06	2.54 \pm 0.30	0.90 \pm 0.06	1.63 \pm 0.20
150	5.32 \pm 0.16	5.62 \pm 0.29	4.20 \pm 0.29	1.85 \pm 0.11	2.11 \pm 0.18
200	8.06 \pm 0.54	8.40 \pm 0.23	7.30 \pm 0.26	4.48 \pm 0.34	3.37 \pm 0.35

^aValues in table are average \pm 1 standard deviation.

As discussed by Tabor (56), initial yielding under a ball indenter occurs at $\approx 1.1Y$, where Y is the yield stress measured in simple uniaxial tension or compression. According to theory, yielding begins to take place at a point $\approx 0.5a$ below the surface directly under the indenter, where a is the contact radius (18). At this location the shear stress is a maximum, given by $\approx 0.48p_0$, where p_0 is the mean contact stress. Only when the mean stress reaches $\approx 3Y$ does all the material begin to yield around the indenter, a condition referred to as “full” plasticity.

From figure 6, the full plasticity condition is taken to occur in the region where the residual depth is linear with the load. Straight line fits through these higher load data points were used to determine the loads for full plastic yielding. This is shown in figure 7, where the x-intercept of the straight lines corresponds to this load. The Hertz equations (equations 1–3 in the appendix) were then used to calculate the mean stress corresponding to these loads. The results are summarized in table 4.

The Vickers hardness of the materials measured at 0.98 N (100 gf), with a 15-s hold time, is shown in the last column in table 4. Residual depth data for the AION is plotted in figures 8 and 9. The transition from elastic to elastic-plastic behavior is more well-defined for AION compared to the glasses. Since AION is a crystalline material, a definite yield stress exists for the movement of dislocations and the formation of mechanical twins, and this may result in a more defined transition point.

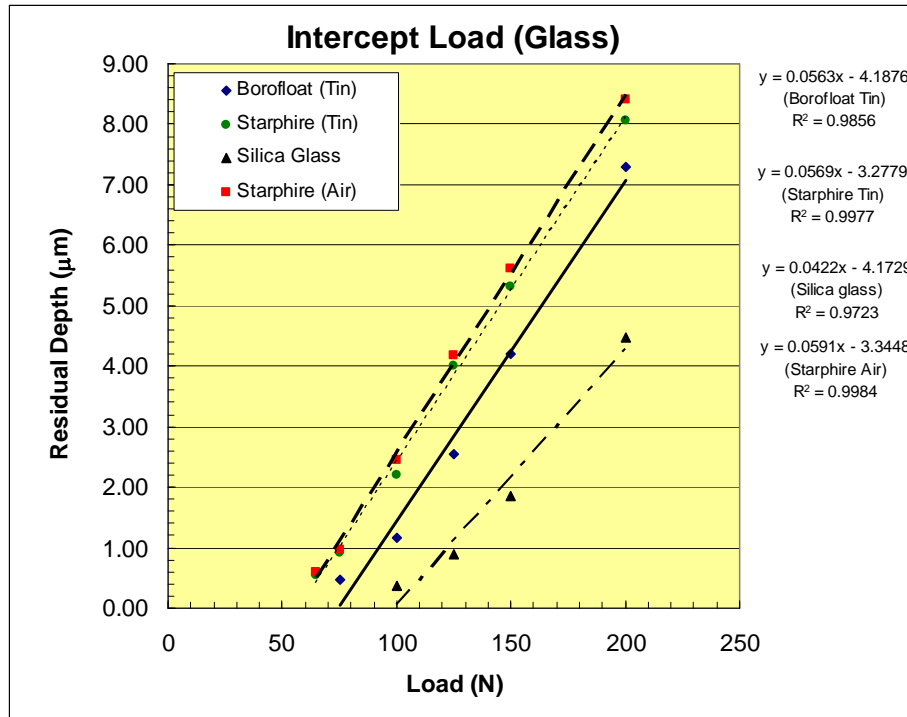


Figure 7. Straight line fits through high-load data points for determining load at “full” plastic yield. The x-intercept marks this load. Error bars are same as in figure 6.

Table 4. Yield data.^a

Material	Yield Load (x-Intercept) (N)	Contact Radius (μm)	Yield Stress (GPa)	Vickers Hardness (GPa)
Starphire (tin)	57.6	53.1	6.5	5.1 ± 0.1
Starphire (air)	56.6	52.8	6.5	4.8 ± 0.1
Borofloat (tin)	74.3	60.7	6.4	5.3 ± 0.2
Silica glass	98.8	63.7	7.8	6.8 ± 0.4
AION	41.9	31.1	13.8	21.3 ± 0.8

^aValues in table are average ±1 standard deviation.

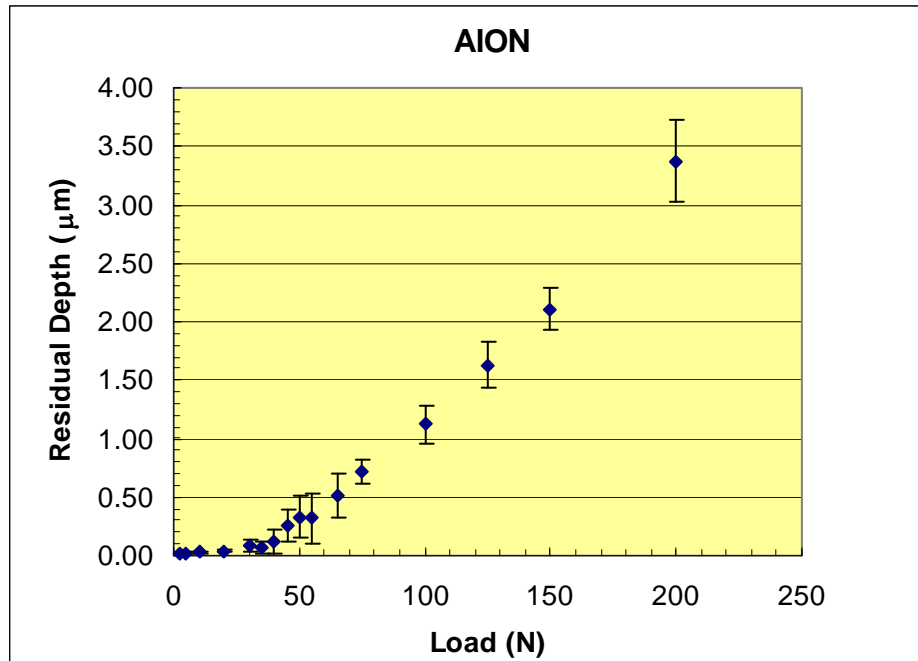


Figure 8. Residual indentation depth as a function of load for AlON using a spherical 500-μm-diameter single-crystal diamond indenter.

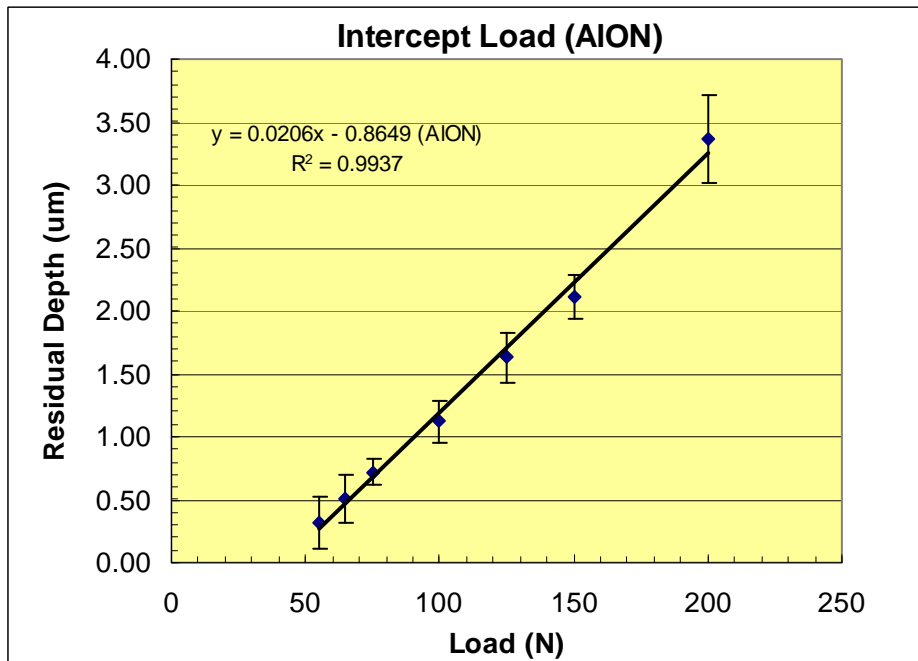


Figure 9. Straight line fit through high-load data points in AlON for determining load at “full” plastic yield.

Both slip and mechanical twinning have been shown to occur in the permanent deformation of aluminum oxide by indentation (51) and hence are also expected to occur in AlON. In table 5, the loads for permanent deformation (dimpling), ring cracking, and radial cracking are shown for the three glasses and AlON based on postmortem observations of the indentation sites.

Table 5. Deformation and fracture loads.^a

Material	Onset Dimpling (N)	All Tests Dimpled (N)	Onset Ring Cracking (N)	All Tests Ring Cracked (N)	Onset Radial Cracking (N)	All Tests Radial Cracked (N)
Starphire (tin)	30	30	65	75	75	100
Starphire (air)	20	30	65	100	100	125
Borofloat (tin)	30	35	30	45	100	200
Silica glass	75	100	20	30	65	75
AlON	35	45	45	65	40	75

^aValues in table are average ± 1 standard deviation.

Loads are listed for both the onset of this behavior and that for which all tests displayed ring cracking, dimpling, and radial cracking. That is, at the onset loads, not all tests may have formed dimples, ring cracks, or radial cracks.

The vitreous silica exhibited ring cracking at a much lower load compared to the Starphire and slightly lower compared to Borofloat. On the other hand, the silica glass had the highest load for which all tests were dimpled, followed by Borofloat, then Starphire. Little difference was seen in the deformation and fracture loads for the air and tin sides of the Starphire glass.

The behavior for the three glasses with increasing load, with respect to the onset of elastic, plastic, and fracture responses, can best be described as (1) Starphire: elastic→plastic→fracture; (2) Borofloat: elastic→plastic and fracture; or (3) silica glass: elastic→fracture→plastic. Note how the silica glass fractures well before yielding, which could be considered a more brittle response compared to the other glasses. For AlON, the trend is elastic→plastic→fracture.

4.1.3 Indentation Damage Patterns

Figures 10–18 show indentation patterns and corresponding load-displacement traces for the three glasses and AlON.

4.1.3.1 Starphire Glass. Figure 10 shows indentation patterns in the tin side of Starphire glass for loads ranging from 35 to 200 N imaged using differential interference contrast (DIC) lighting conditions on an optical microscope. At loads from 2 to 20 N, no visual damage (cracking or dimpling) was seen in the glass.

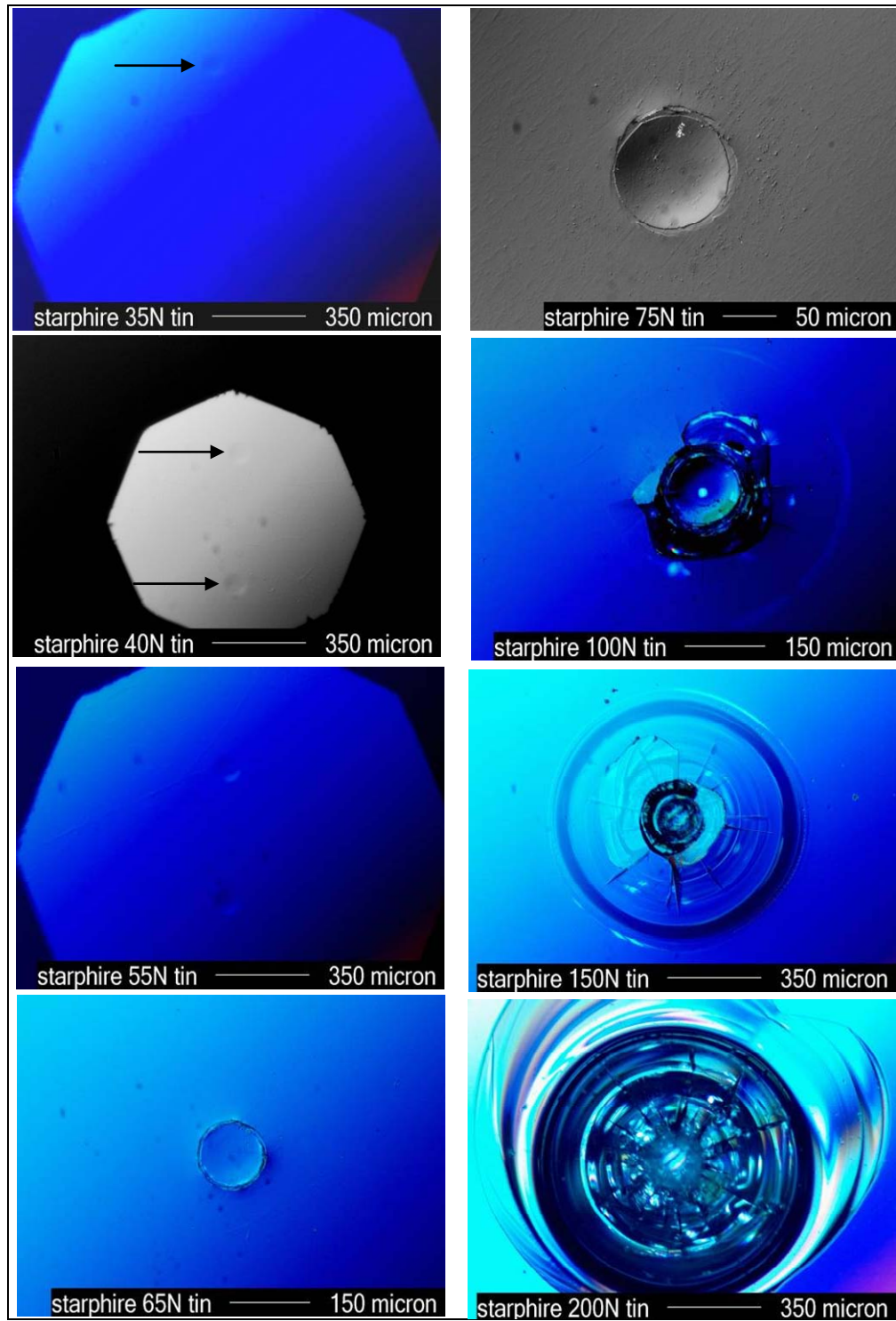


Figure 10. Indentation sites in the tin side of Starphire glass produced with spherical 500- μm -diameter single-crystal diamond indenter.

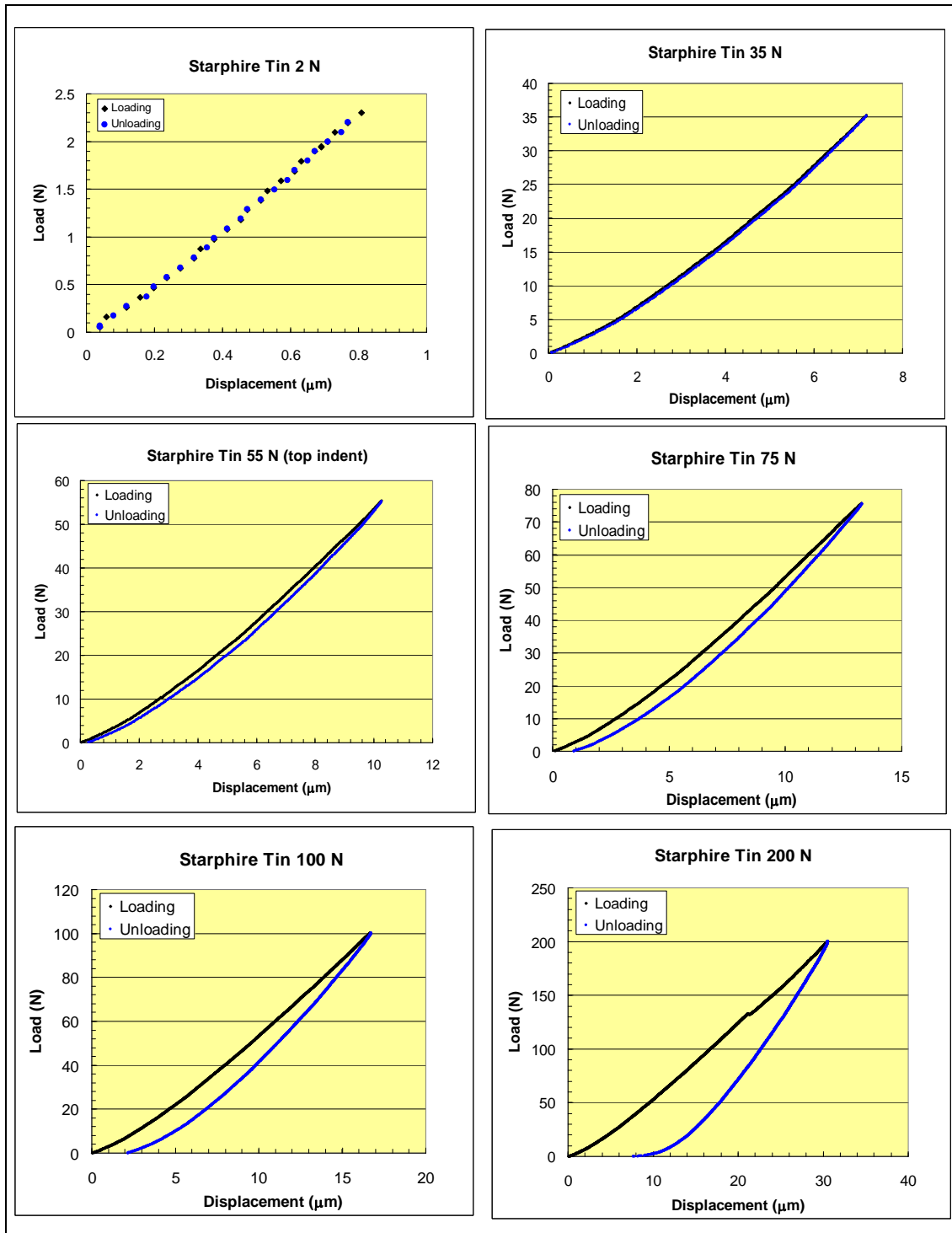


Figure 11. Load-displacement traces for the tin side of Starphire glass. The curves correspond to the same indentation sites shown in figure 10. Curves produced with spherical 500- μm -diameter single-crystal diamond indenter.

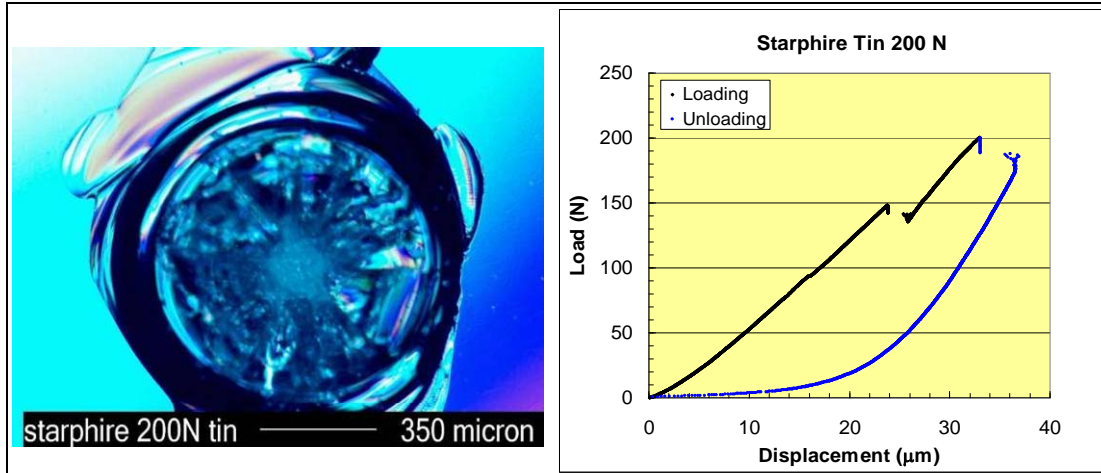


Figure 12. The 200-N indentation site in tin side of Starphire glass and corresponding load-displacement trace for test showing catastrophic failure under indenter. The 500- μm -diameter spherical diamond indenter used.

The data in table 3 supports these observations for loads up to 10 N, taking the experimental scatter into account, where the residual depth is within the limits of detectability of the measuring system; recall the resolution of the displacement measuring system was given as 0.02 μm by the manufacturer.

At 30 N, table 3 shows the residual depth to be $0.07 \pm 0.01 \mu\text{m}$. These 30-N dimples were just visible in the glass; however, these could not be seen on a digital image. At 35 N, the dimples could be imaged (see figure 10). Note that although the residual depth is $0.10 \pm 0.02 \mu\text{m}$, i.e., below the wavelength of visible light, the widths of the dimples are expected to be at least twice the depths, and thus begin to be on the cusp of visual detection. The DIC illumination method also enhances the detectability by increasing resolution, since the dimples up to 45-N load were not seen using ordinary bright-field imaging.

Load-displacement traces for this glass are shown in figure 11. For loads above 100 N, discontinuities (jogs) were observed in the load-displacement traces corresponding to the initiation of a large ring-cone crack and/or massive failure below the indenter. The latter would produce a loud audible pop, at which point a drastic discontinuity was seen. This was believed to correspond to massive failure below the indenter, where the compressive strength of the glass was exceeded. An example is illustrated in figure 12. Note how the residual depth goes to zero. This is believed to be due to the pulverized material occupying a non-negligible volume due to dilatation, which pushed back on the indenter. The 200-N indentation in figure 10 contains a small region at the center that is intact, whereas the one in figure 12 does not, thus supporting this hypothesis.

4.1.3.2 Borofloat Glass. Figure 13 shows indentation patterns on the tin side of the Borofloat glass. The dimples were more difficult to observe compared to the Starphire glass, partly because they were shallower. The indentation at 65 N shows that the region of dimpling is significantly smaller than the ring crack radius. Since ring cracks tend to initiate just outside the contact radius, it is clear that a condition of full plastic flow has not been achieved, otherwise the dimple should extend to near the edge of contact.

At 75 N, the dimple is seen to extend to a larger fraction of the contact radius, closer to a condition of full plasticity. However, compared to the Starphire glass, the dimple is still not as well developed. These observations support the higher intercept load observed for this glass compared to Starphire. Although the stress level for full plasticity is nearly the same for both glasses, it takes a higher load to reach this stress level compared to the Starphire glass (see table 4).

More severe surface spalling also occurred for this glass compared to Starphire (see 150-N indentation). Radial cracks were observed for loads of 100 N and above but tended to be obscured by the surface spalling. These cracks were shorter compared to Starphire glass, indicating a tougher glass.

Load-displacement traces for the Borofloat are shown in figure 14. Small discontinuities (jogs) in these curves were frequently observed for the higher load tests and are believed to result from the initiation of particularly severe ring-cone cracks.

4.1.3.3 Silica Glass. Figure 15 shows indentation patterns in the vitreous silica glass as a function of load. In this glass, cracking occurred well before the presence of permanent deformation could be observed. The 200-N indentation site is shown in transmitted light, which highlights the extensive cracking that occurred, including the well-developed radial cracks.

Discontinuities in the load-displacement curves tended to occur at lower loads and appear in more tests compared to the other glasses. Figure 16 shows plots of the load-displacement curves for this glass.

4.1.3.4 AlON. In figure 17, indentation sites are shown for the AlON material for loads ranging from 35 to 200 N. Because the average grain size of the AlON is very large, i.e., $\sim 150\text{ }\mu\text{m}$, the indentations are primarily within single grains, especially for the lower loads. In addition, the cracks are likely contained within single grains, except perhaps at the higher loads, e.g., 200 N, where the cracks might span several grains.

Because the indents lie primarily within single grains, anisotropies in cracking behavior were observed, despite AlON being cubic. This is because the crystallographic orientation of the indented faces of the grains is different and influences the fracture behavior. Twinning has been shown to occur on the fracture surfaces of AlON test specimens (43), and deformation twins can also be seen within many of the indentations in figure 17. Figure 18 shows indentation sites in AlON as a function of load.

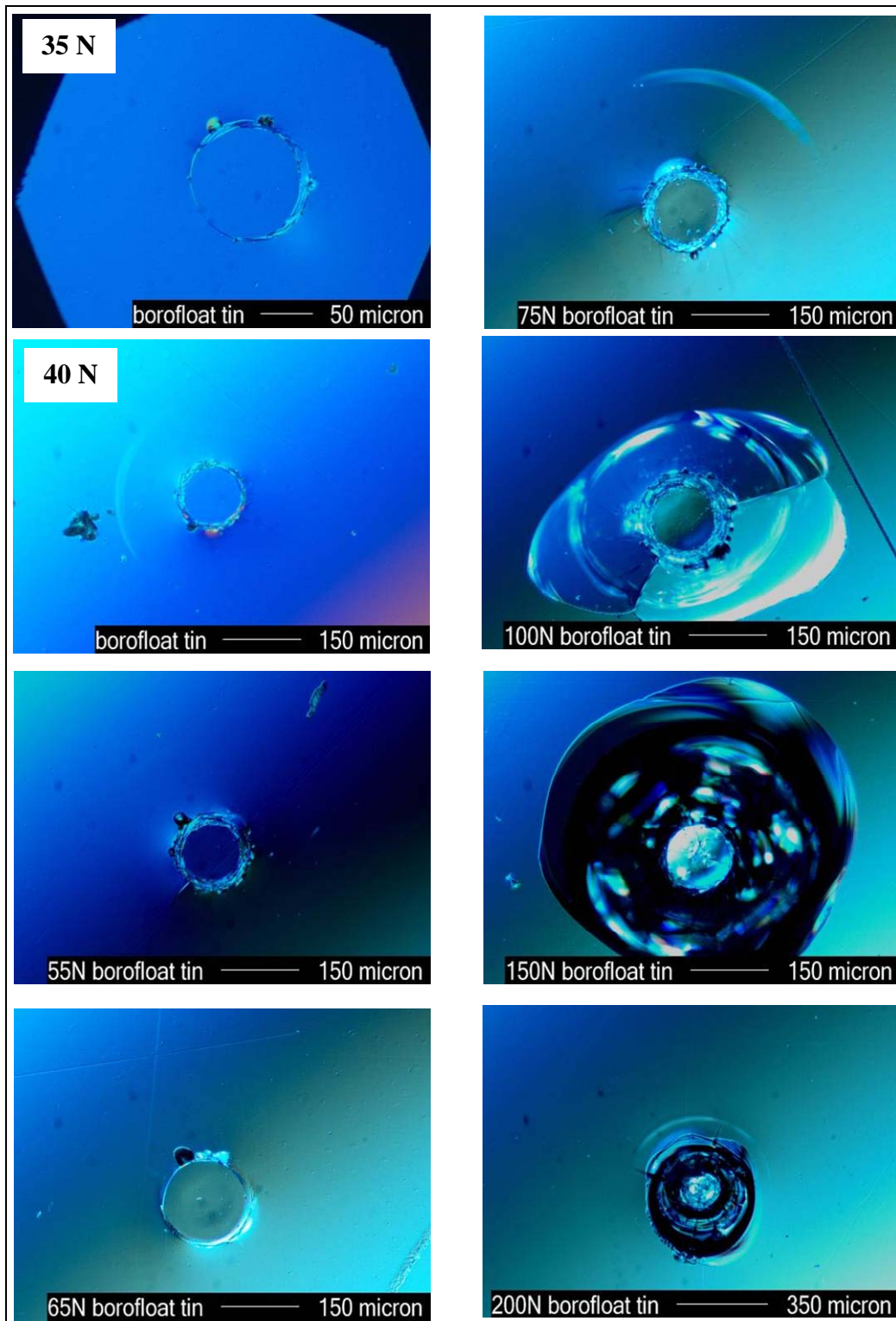


Figure 13. Indentation sites in the tin side of Borofloat glass produced with spherical 500- μm -diameter single-crystal diamond indenter.

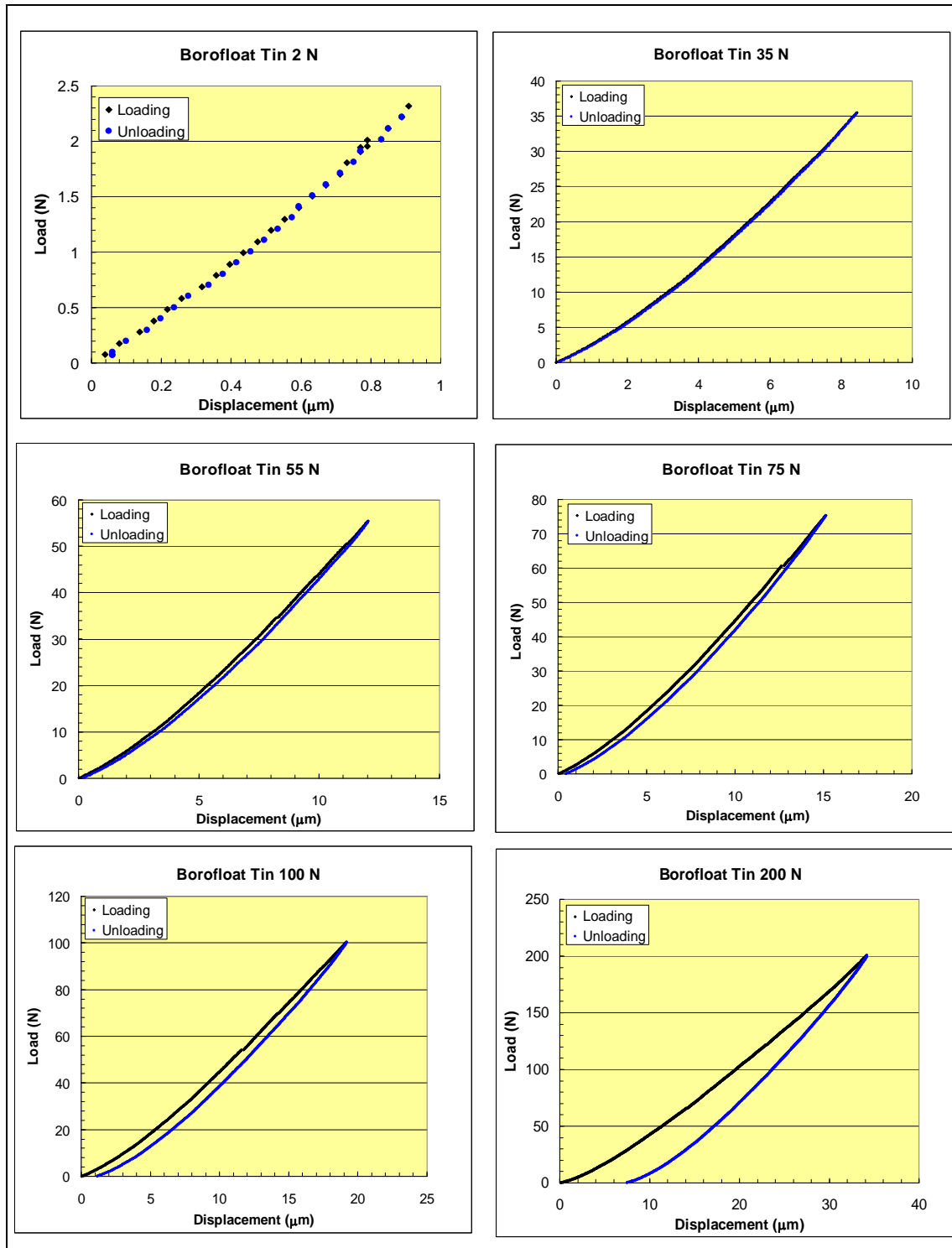


Figure 14. Load-displacement traces for the tin side of Borofloat glass. The curves correspond to the same indentation sites shown in figure 13. Curves produced with spherical 500- μm -diameter single-crystal diamond indenter.

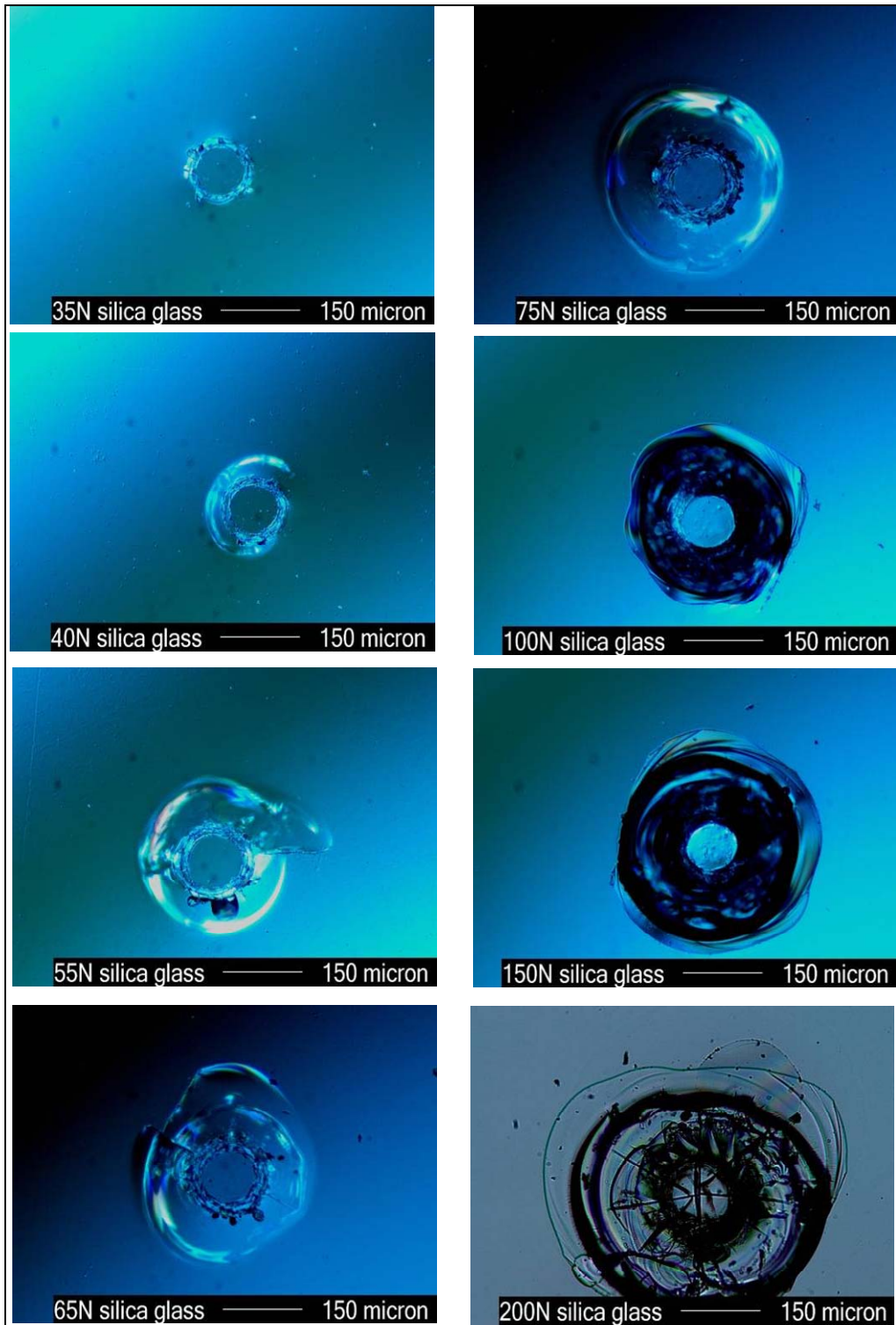


Figure 15. Indentation sites in silica glass produced with spherical 500- μm -diameter single-crystal diamond indenter.

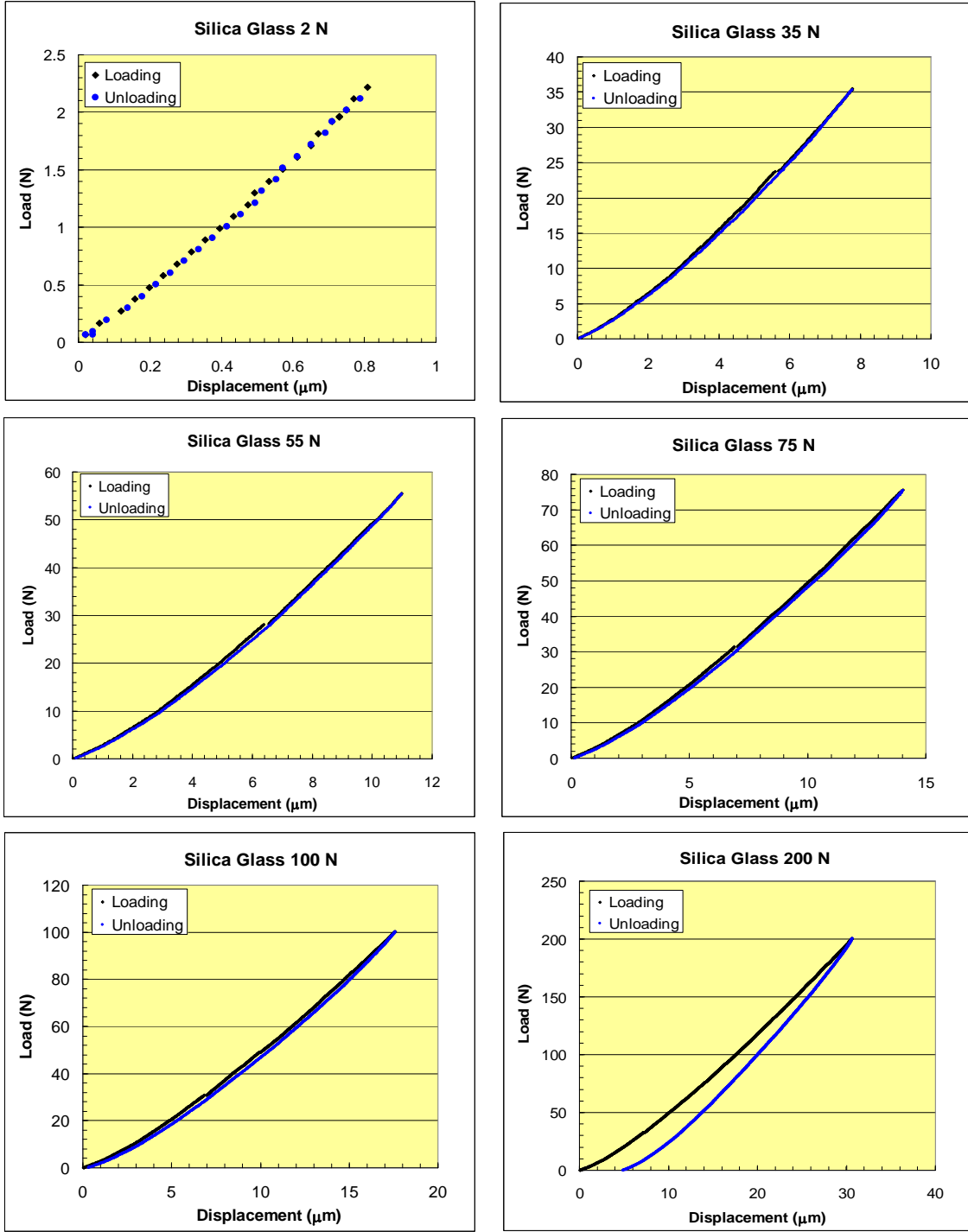


Figure 16. Load-displacement traces for the silica glass. The curves correspond to the same indentation sites shown in figure 15. Curves produced with spherical 500- μm -diameter single-crystal diamond indenter.



Figure 17. Indentation sites in polycrystalline AlON produced with spherical 500- μm -diameter single-crystal diamond indenter.

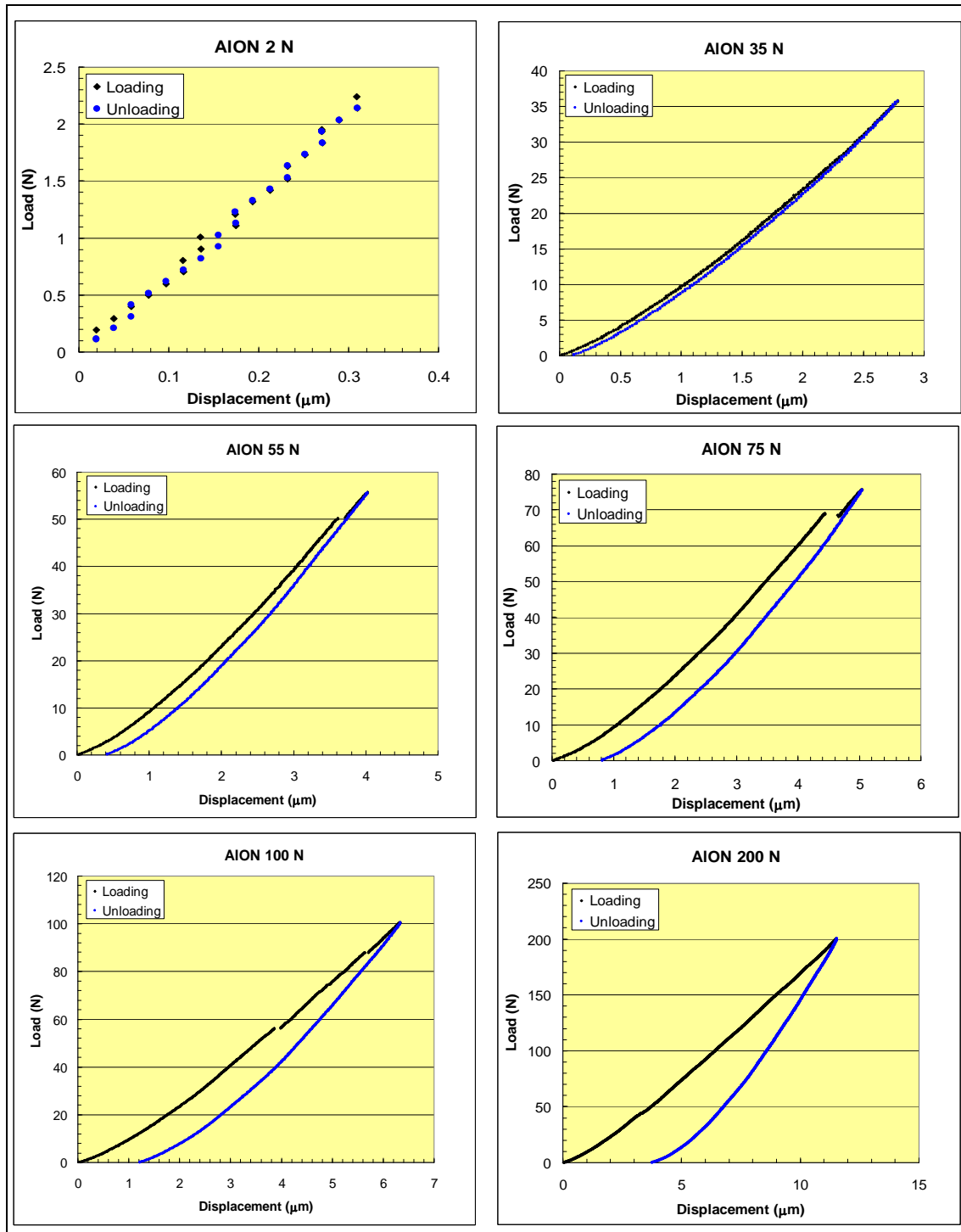


Figure 18. Load-displacement traces for AION. The curves correspond to the same indentation sites shown in figure 17. Curves produced with spherical 500- μm -diameter single-crystal diamond indenter.

Figure 19 shows a good example of deformation twinning within a 150-N indentation. In addition to slip, twinning in crystals is another way to achieve irreversible deformation. The dark bands represent shear failure of material because of twin formation. That is, the material twins and then fails along the twin.

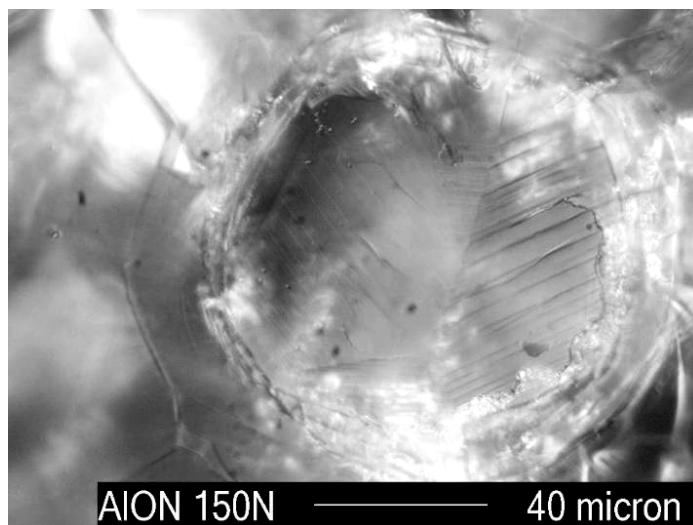


Figure 19. An example of deformation twinning inside a 150-N indentation in AlON produced with 500- μm -diameter spherical diamond indenter.

Twinning results from homogeneous shear deformation in which the crystal changes shape at fractions of the atomic displacement (Burgers) vector in all planes, in comparison to slip where movement occurs in multiples of the Burgers vector along specific planes. Twinning also differs from dislocation slip in that a reorientation of the lattice takes place, where twinned atoms are a mirror image of those in the untwinned material. In dislocation slip, the lattice orientation remains essentially unchanged after the dislocation passes through (58).

4.1.4 IIT Load-Displacement Data Analysis

The load-displacement data was examined for each of the materials with respect to the maximum displacement and elastic recovery of the indentations in the vertical (depth) direction. The results are plotted in figures 20–22. The elastic recovery is seen to increase for all materials with increasing maximum load, as seen in figure 20.

The Borofloat glass showed the most elastic recovery, followed by silica glass, Starphire, and then AlON. However, when the percent elastic recovery is plotted, the silica glass has the greatest percentage elastic recovery, followed by Borofloat, Starphire, and then AlON.

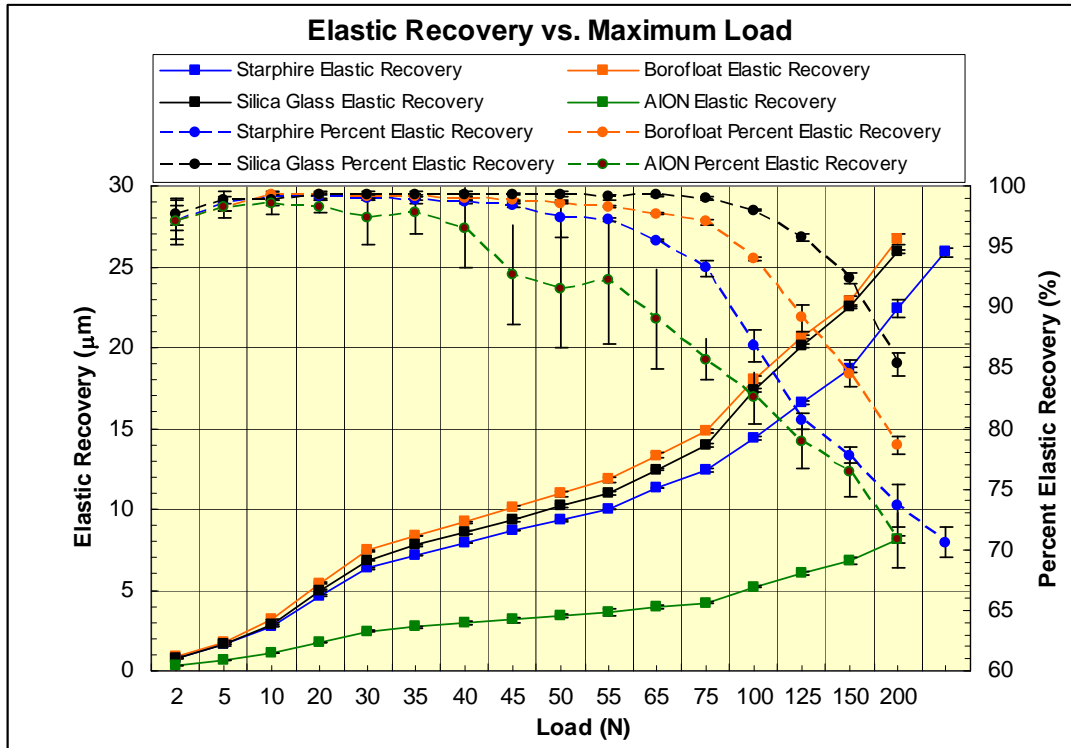


Figure 20. Elastic recovery and percent elastic recovery as a function of the maximum indentation load for glass and AION materials. Data for tin sides are plotted for Starphire and Borofloat glasses.

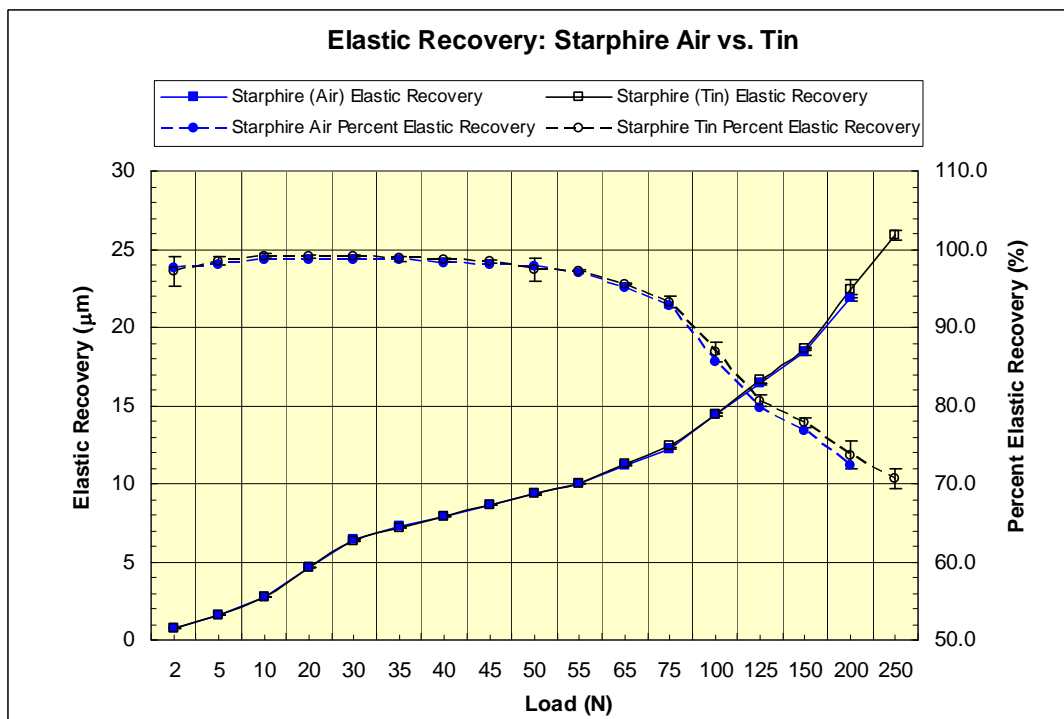


Figure 21. Comparison of elastic recovery behavior of tin and air sides of Starphire glass.

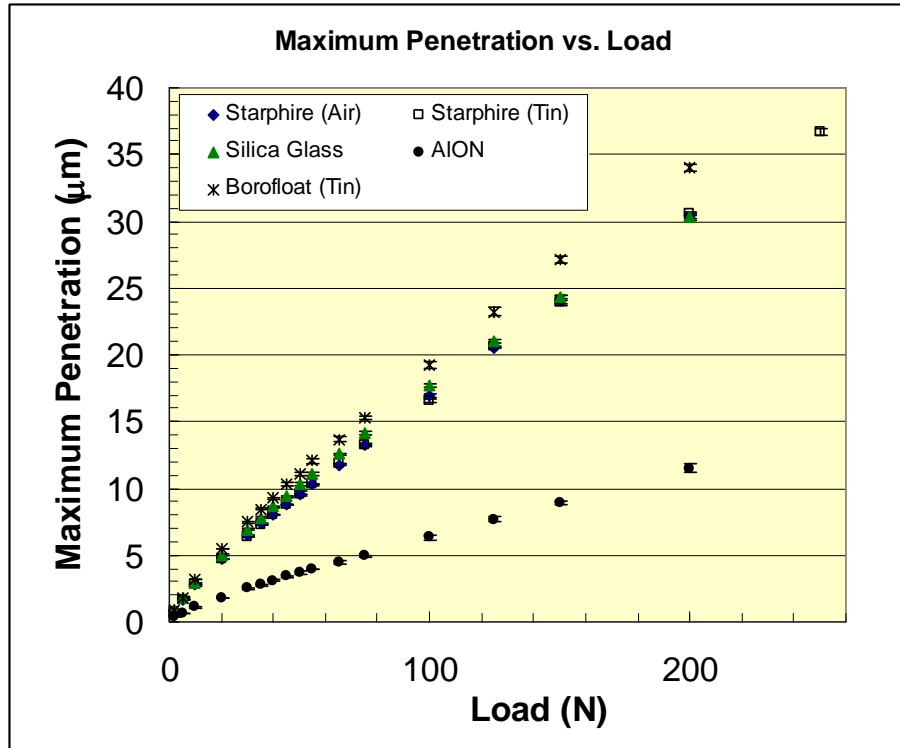


Figure 22. Maximum penetration depth as a function of load for the three glass materials and AION.

Figure 21 shows there is no significant difference between the air and tin sides of the Starphire glass in terms of elastic recovery behavior. One may note the air side shows slightly more percent elastic recovery compared to the tin side.

In figure 22, the maximum penetration is shown as a function of the load for all materials. The Starphire and silica glasses showed similar behavior, and no significant differences between the air and tin sides of the Starphire are apparent.

The Borofloat showed slightly higher penetration compared to the silica and Starphire glasses. The higher silica content of the Borofloat glass compared to Starphire yields a more open structure capable of deforming more under load, despite the fact these glasses had similar Vickers hardness (the greater elastic recovery behavior of the Borofloat may cause more contraction of the diagonals in a conventional Vickers indentation test, leading to similar Vickers hardness).

Although the silica glass has the most open structure of the glasses, it has a stronger connected network due to the lack of modifier ions and hence shows less penetration under load compared to Borofloat, consistent with its higher Vickers hardness.

The AION showed the least penetration with load, consistent with its strong intrinsic bonding compared to the glasses, as evidence by its high Vickers hardness.

4.1.5 In-Situ Crack Initiation Observation

Experiments were conducted on all three glass materials and AlON in which the formation of cracks was observed in real time via a unique test configuration that was set up on the IIT tester. A picture of the test arrangement is shown in figure 23.

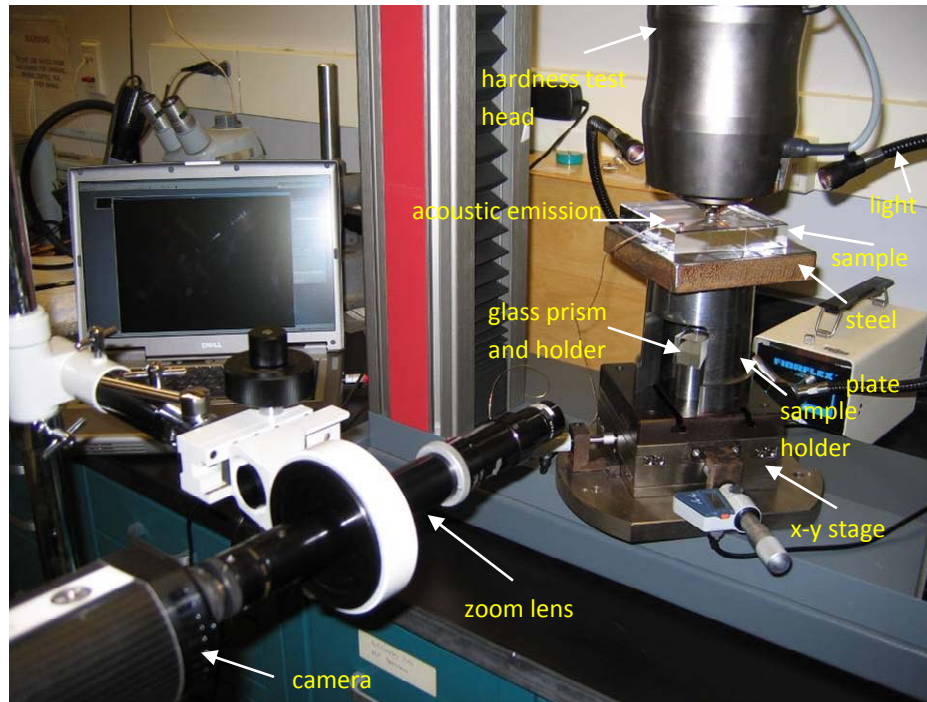


Figure 23. Experimental setup for observing the crack initiation behavior of transparent materials in real time with the IIT system.

The specimen rested on a 1-in-thick steel plate that had a 0.75-in-diameter hole in the middle to allow light to pass through to the glass prism below. The glass prism redirected the light 90° into the zoom lens and camera system. A laptop computer and software allowed observation and recording of the entire contact process from below. The steel plate was in turn supported by the steel sample holder, which was hollow in the middle with a 3-in-diameter support radius.

The thick steel plate and small circular hole helped ensure rigid specimen support. An acoustic emission sensor was attached to the specimen with super glue to record any activity. The acoustic emission (AE) system also recorded the load from the IIT tester, so the initiation load was recorded for each hit produced.

Twenty tests were conducted, with a maximum load of 150 N and a displacement rate of 1 $\mu\text{m/s}$ on both loading and unloading. Table 6 summarizes the crack initiation behavior. Parentheses indicate the percentage of tests in which that behavior was observed.

Table 6. Crack initiation summary.^a

150-N Max. Load	Loading Cycle			Unloading Cycle	
Material	Ring/Cone Cracking (N)	Radial Cracking (N)	Lateral Cracking (N)	Radial Cracking (N)	Lateral Cracking
Starphire (tin)	39 ± 8 (100%)	No	No	74 ± 3 (100%)	Yes
Starphire (air)	76 ± 10 (100%)	No	No	71 ± 7 (100%)	Yes
Borofloat (tin)	50 ± 20 (100%)	60%	No	27 ± 18 (100%)	Yes
Borofloat (air)	60 ± 29 (100%)	55%	No	25 ± 9 (100%)	Yes
Vitreous silica	24 ± 9 (100%)	24 ± 9 (100%)	No	48 ± 12 (100%)	Yes
AION	56 ± 17 (100%)	(70%)	No	(100%)	Yes

^aValues in table are average ±1 standard deviation.

All materials had ring-cone cracks initiate on loading. There was a substantial difference in initiation loads between the tin and air sides for the Starphire glass but not much difference between these sides for the Borofloat. The air side of the Starphire was slightly more resistant to ring-cone cracking than the air side of the Borofloat, but the opposite was true for the tin sides. The vitreous silica was least resistant to ring-cone cracking of all the glasses.

The reason for the rather large discrepancy in ring cracking loads in the tin side of Starphire between the postmortem observations of cracking conducted from the yield stress tests (table 5), i.e., 65 N, and the in-situ measurements, i.e., 39 N, is puzzling, particularly since no significant differences were seen between the air sides from the two test techniques. One possibility is that the tin side of the sample was unintentionally, and unknowingly, handled roughly after the yield stress tests, introducing more severe surface flaws that caused the ring crack initiation loads to decrease.

The AION material initiated ring-cone cracks on loading, but the overall extent of cone crack formation was unclear. In addition, the silica glass, Borofloat, and AION materials had radial cracks initiate on loading. For the silica glass, the radial cracks that initiated on loading did so simultaneously with the ring-cone cracks that initiated. Radial cracks were seen to initiate in 100% of the tests for silica glass and 70% of the tests for AION.

For the Borofloat glass, radial cracks initiated on loading for about half the tests, primarily at loads higher than the load needed to initiate the first ring-cone crack. For all the glasses, the unloading cycle began with the cone crack retracting significantly, but not all the way, and was particularly pronounced for the silica glass. This occurred before the initiation of any radial cracks on unloading. Some retracting of the cone crack in the AION was seen as well, though it did not appear as pronounced as for the glasses. Radial cracks initiated in all materials on unloading; however, for the Borofloat glass only 55% and 60% of the tests had these cracks initiate, corresponding to the air and tin sides, respectively, and were the same tests that formed these cracks on loading.

For the Borofloat and silica glasses, the radial cracks that formed on loading would tend to retract slightly on unloading, which was then followed by the initiation of additional radial cracks. For the Starphire glass, a drastic cracking event took place on unloading corresponding to the partial detachment of the top one-third of the cone crack from the rest of the cone crack. This event was accompanied simultaneously by the initiation of the radial cracks and is believed to result from the large elastic mismatch between the “plastic” zone and surrounding elastic material.

This type of behavior was significantly reduced in the Borofloat, and especially the silica, glasses because of the lower elastic mismatch. This is because these glasses have a more open network structure and fewer modifying cations, and hence undergo less shape change beneath the indenter. This results in less elastic mismatch and a less intense residual crack opening force compared to Starphire glass, where the greater amount of modifier ions allows more shear flow to take place, which increases the mismatch.

The loads at which radial cracks formed in the AION could not be determined accurately due to the translucent nature of the AION. On the unloading half-cycle, the formation of radial cracks at lower loads indicates an increased resistance to cracking. This is because as the indenter is removed and the load decreases, the net tensile stress at any fixed location near the surface increases as the elastic compressive stresses continually diminish.

Thus, the Starphire glass had the greatest resistance to radial cracking on loading, since no cracks formed. However, on unloading, the Borofloat and silica glasses had greater resistances to radial cracking, since these cracks formed at lower loads compared to Starphire. Lateral cracks formed in all materials near or just after complete load removal.

4.1.5.1 In-Situ Indentation Patterns. Figure 24 shows indentation sequences on the tin sides of the Starphire and Borofloat glasses. Frames (a) represent contact of the indenter just before ring/cone crack initiation. Frames (b) correspond to the exact moment the ring/cone crack popped in. The diameter of the cone crack is much larger in the Borofloat glass because the average initiation load was greater in the Borofloat tin side compared to the Starphire tin side (see table 6), hence the cone crack grew larger at the moment of initiation in the Borofloat glass.

Frames (c) correspond to the maximum load (150 N). Two small radial cracks can be seen in the Borofloat glass, shown by the two small white arrows in this picture. Frames (d) represent complete unloading of the indenter, which is when the load is zero. The radial cracks are apparent in the Starphire glass in this frame. Radial cracks are seen in the Borofloat, but they are smaller due to this glass’ slightly higher toughness and reduced residual crack driving force compared to Starphire.

Figure 25 shows indentation sequences in silica glass and AION. Radial cracks are visible in the silica glass at the moment of ring/cone crack initiation, as seen in frames (c). The cracking behavior of the AION was less pronounced in this example, probably because of anisotropy,

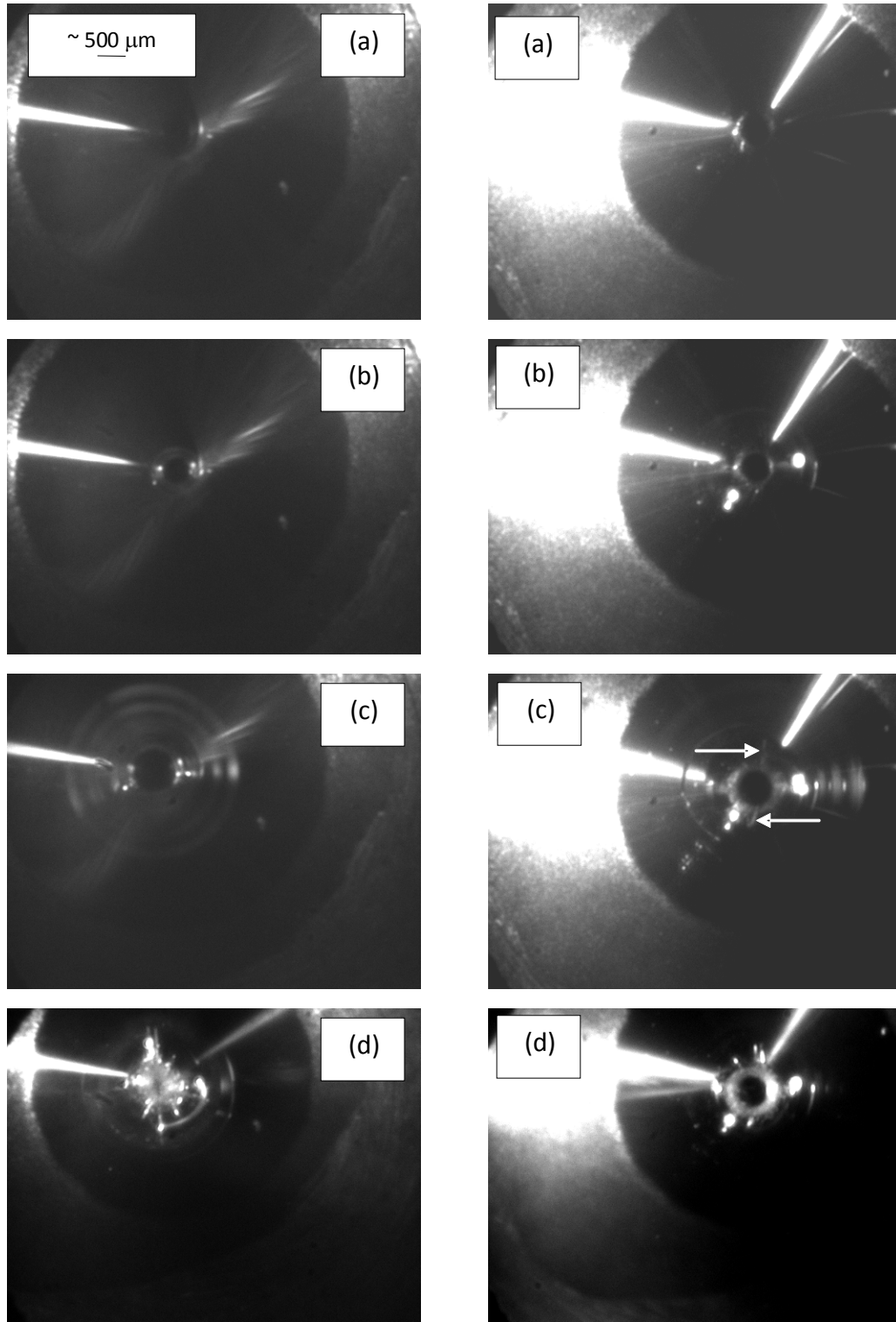


Figure 24. In-situ indentation patterns in the tin sides of Starphire (left) and Borofloat (right) glasses: (a) $F < F_c$, (b) $F = F_c$, (c) $F = F_{\max} = 150$ N, and (d) complete unloading ($F = 0$ N) ([a–c] loading cycle and [d] unloading cycle).

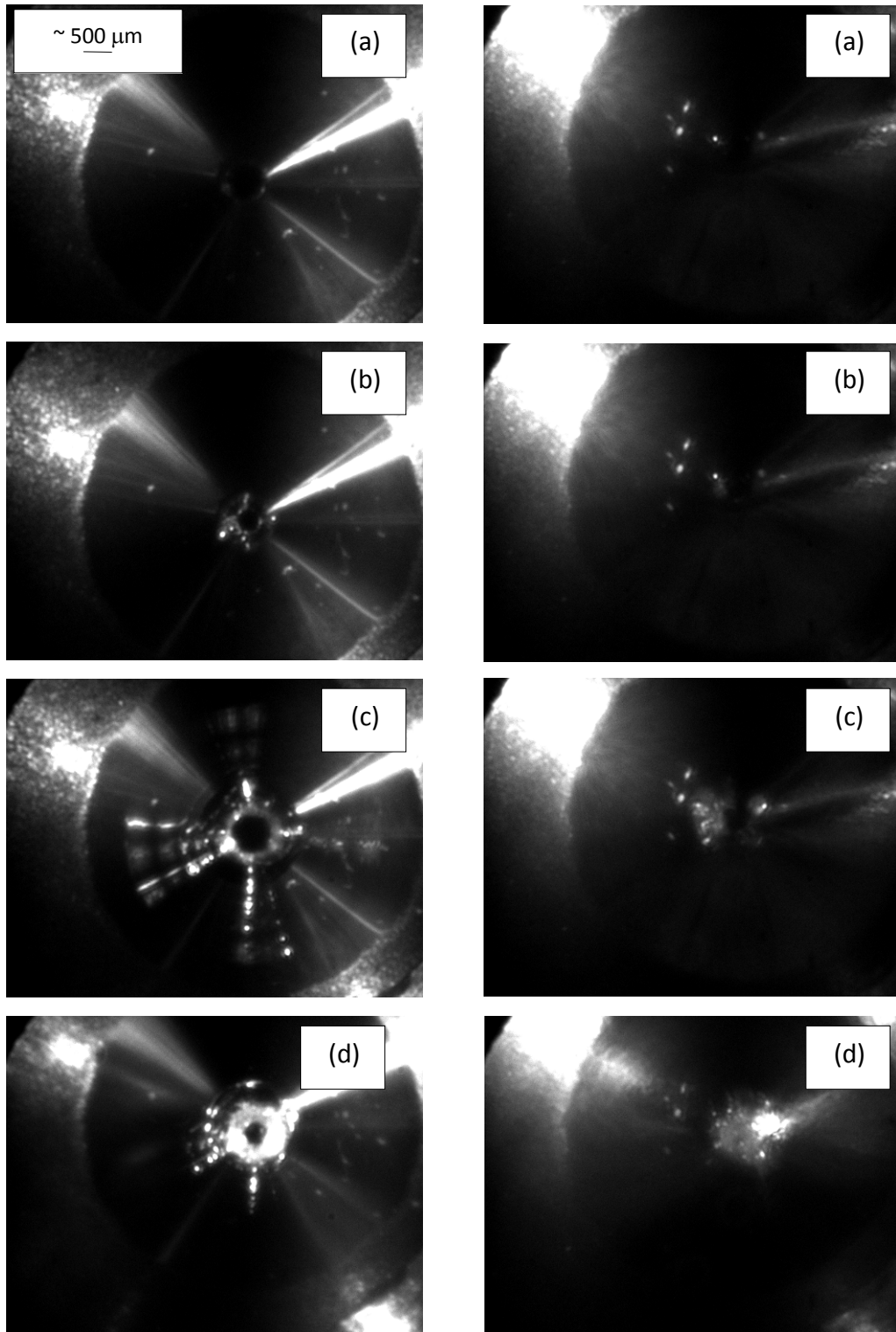


Figure 25. In-situ indentation patterns in silica glass (left) and AlON (right): (a) $F < F_c$, (b) $F = F_c$, (c) $F = F_{max}$, and (d) complete unloading ($F = 0$ N) ([a–c] loading cycle and [d] unloading cycle).

resulting from the indentations being on the order of the grain size or smaller. In addition, the AlON was not fully transparent but was slightly cloudy, which further reduced the clarity of the images compared to the glasses.

4.1.5.2 Acoustic Emission Data. Table 7 summarizes the acoustic emission hit and energy data from the crack initiation experiments. In AE, what is being monitored is the sensor's electrical response to a mechanical stimulus, not the actual stimulus itself. Hence, factors such as the degree of coupling between the sensor and the test material could potentially affect the results.

Table 7. Acoustic emission data.^a

Material	Hits Loading	Hits Unloading	Total Hits	Energy Loading	Energy Unloading	Total Energy
Starphire (tin)	25 ± 10	7 ± 3	31 ± 10	259 ± 114	180 ± 45	439 ± 127
Starphire (air)	103 ± 37	12 ± 4	103 ± 37	904 ± 363	185 ± 49	1032 ± 366
Borofloat (tin)	39 ± 14	5 ± 6	44 ± 13	1449 ± 261	65 ± 95	1514 ± 263
Borofloat (air)	90 ± 37	12 ± 6	101 ± 37	2957 ± 787	99 ± 67	3056 ± 791
Vitreous silica	83 ± 21	6 ± 4	88 ± 23	1415 ± 232	79 ± 73	1493 ± 275
AION	21 ± 6	1 ± 1	22 ± 6	350 ± 237	4 ± 9	354 ± 238

^aValues in table are average ±1 standard deviation.

In this work, a cyanoacrylate-based, fast-acting adhesive was used to couple the sensor to the surfaces of the specimens. All AE parameters were kept the same for all materials. The energy data is in arbitrary units. Relative comparisons between materials are sought.

A hit refers to a more-or-less discrete signal detected and processed by the AE computer, and to a first approximation the total hit amount can be thought to represent the overall activity occurring in the material. The energy measurement is a function of the amplitude and duration of a hit and thus indicates the intensity of a hit.

The data show that the air sides of the Starphire and Borofloat glasses were considerably more active than the tin sides, possibly suggesting a greater amount of deformation and microcracking activity on the air sides. In addition, this difference in activity primarily arose on the loading cycle, since the unloading cycles showed much less difference in the number of hits between the air and tin sides.

Whereas the hits on loading arose from the initiation of ring-cone cracks and possibly other smaller microcracking events, e.g., material crushing between surface ring cracks, the unloading hits were generated by the initiation of radial and lateral cracks.

One may thus expect to see a difference between the surface ring cracking behavior between the air and tin sides of these two glasses; however, posttest microscopy was unable to reveal any differences above the normal test-to-test variations typically seen.

This is illustrated in figure 26 for Starphire glass, which shows 150-N indentation sites on both the tin and air sides. One possible explanation is that the stress waves are carried more intensely (that is, with less attenuation) on the air side than the tin side, allowing more higher-intensity signals to pass the threshold requirement for detection.

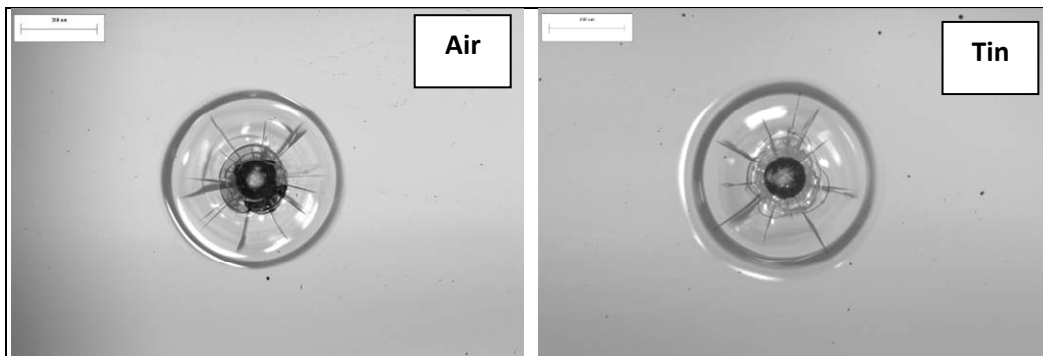


Figure 26. The 150-N indentation sites in Starphire glass for both air and tin sides made with 500-μm-diameter spherical diamond indenter.

4.2 Structural Failure Experiments

Square tiles of the Starphire glass with nominal dimensions of 4×4 in with thicknesses of 3.2, 6, and 12 mm were used in the structural failure tests. The tiles were cut from larger sheets of glass by Swift Glass Company (Elmira, NY). The eight side edges of the tiles and the four corner edges were beveled smooth by Swift Glass in order to minimize the probability of the tiles failing from edge defects left over from the tile cutting process.

In these tests the tiles were centrally loaded with hardened steel spheres (McMaster Carr Bearing-Quality Aircraft-Grade E52100 Alloy Steel; Grade 25; ± 0.001 -in-diameter tolerance; ± 0.000025 -in sphericity; 295,000-psi (2.03-GPa) yield strength; Rockwell Hardness C60-67) while being supported by the same 3-in-diameter circular sample holder used in the crack initiation tests.

A picture of the assembly is shown in figure 27. Three steel alignment rods ensured the tiles were loaded at their center, two of which are shown labeled in figure 25. The third rod is behind the sample holder. The sample holder rested on an x-y stage, which allowed further fine-tuning of the alignment if necessary. The sample holder was fastened to a steel plate that was fastened to the x-y stage, which allowed no movement of the sample holder during testing.

The whole assembly was attached to the piston of the Instron 1332 hydraulic testing machine through several additional pieces. The sample holder was made from 17-4 steel, which can be (precipitation) hardened if desired. The holder was not hardened in case further machining modifications were deemed necessary after testing was complete. The indenter holder and other fixtures made from 17-4 steel were hardened and turned a dark bronze color from the hardening process.

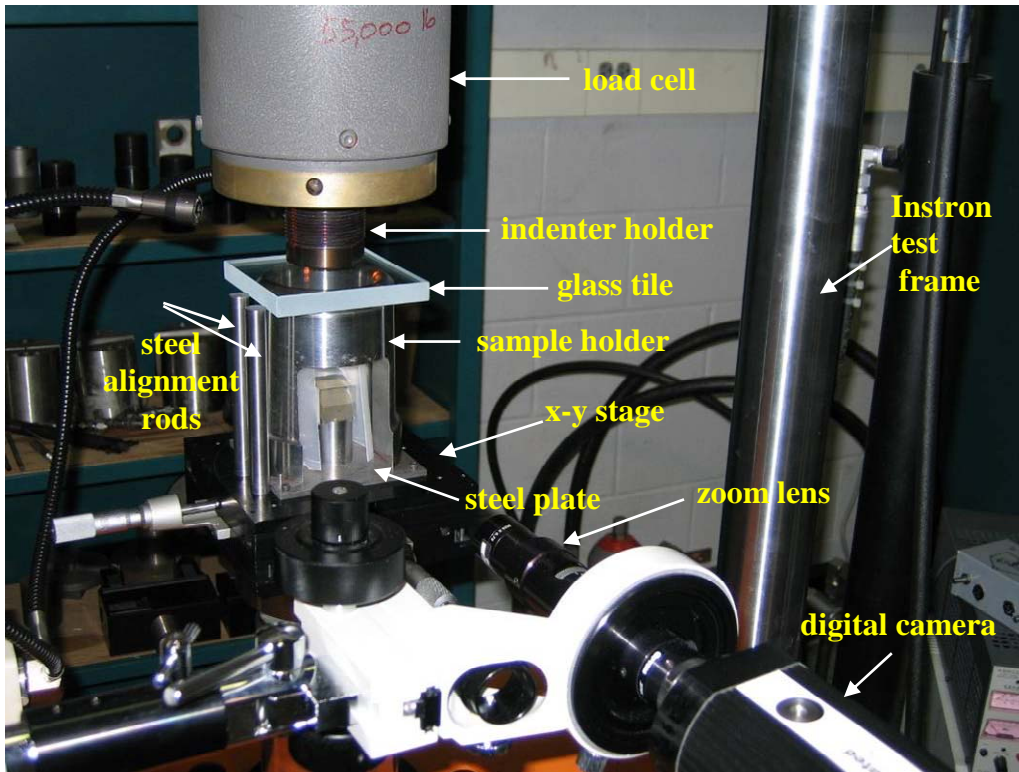


Figure 27. Picture of the experimental setup used to study the structural failure behavior of the tiles.

The steel balls were held in place by semicircles machined into the indenter holders, which were the depth of one-half of the ball diameter. Each diameter ball had its own holder. A small amount of superglue held the balls in place. The only exception was the 1.5-in-diameter ball, which did not have its own holder. The 0.75-in holder was used to hold this ball in place.

Not visible in the picture is the hydraulic piston that moved the specimens up into the stationary steel ball at a rate of 0.5 mm/min. Any cracks that initiated could be observed with the optical setup, as previously described.

4.2.1 Tile Preparation and Testing

The majority of the tiles tested were abraded with SiC particles on both the air and tin sides to try and ensure a more-or-less uniform flaw size distribution. A set of tiles was also tested in the as-received condition in order to determine the effect of the abrasion treatment.

The tiles were abraded by lapping with 220-grit SiC powder (K.C. Abrasive Company, Kansas City, KS) for 4 min on both sides. According to the supplier, this grit size corresponded to $\sim 63\text{-}\mu\text{m}$ average particle size.

A stopwatch was used to keep track of time. A 12-in-diameter circular sheet of 1200-grit ($\sim 3\text{-}\mu\text{m}$ average grain size) SiC paper was placed on the aluminum rotating wheel, and then the 220-grit SiC powder was sprinkled on top and tap water added as a lubricant. A 100-rpm wheel speed was used.

The fine SiC paper was used to protect the softer aluminum wheel from becoming damaged by the loose abrasive SiC powder. Note that since the SiC grains on the paper were much smaller than the 220-grit SiC powder, they did not cause the major abrasive damage. The tiles were rotated 90° every minute, and additional water was added when needed. Tiles were cleaned with isopropyl alcohol after abrasion.

Figure 28 shows a Starphire tile both before and after abrasion, for both tin and air sides. The damage consists of scratches/cracks and small chips on the surface. Tiles were aged overnight in laboratory air and tested the following day. One set of tiles was prepared and tested at a time.

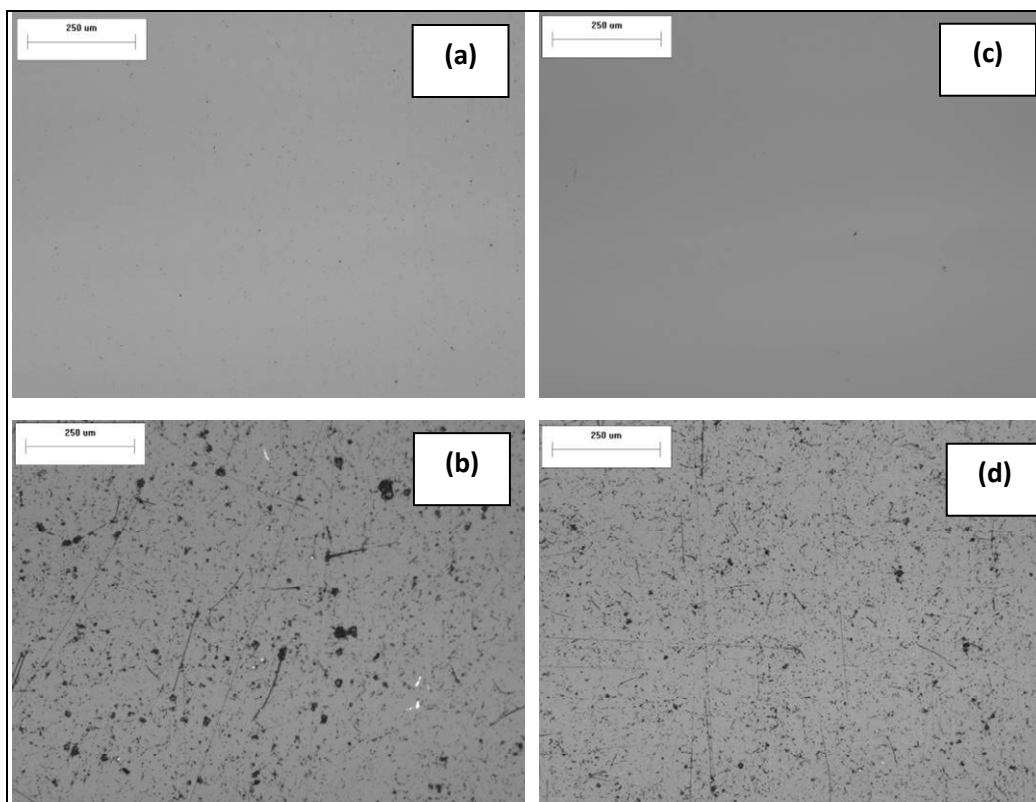


Figure 28. Starphire tile both as-received and after 220-grit abrasion: (a) as-received air side, (b) after abrasion air side, (c) as-received tin side, and (d) after abrasion tin side. All images $250\times$ original magnification.

Temperature and relative humidity were monitored at all times. Tiles were cleaned with isopropyl alcohol on both sides prior to testing but before taping. The tin sides of the samples were loaded with the steel ball, with the air sides facing down and in tension. This was true for all tests.

In order to hold the tiles together after failing, clear plastic tape was placed on the compression (top) surface before testing. The tape was arranged in four strips, and the center of the tile was free of tape such that the steel ball only contacted the glass. The amount of tape used was kept constant for each tile. The actuator displacement rate was 0.5 mm/min for all tests. When failure occurred, the test was stopped.

4.2.2 Failure Test Results

4.2.2.1 3.2-mm Tiles. Table 8 summarizes the failure test results. Figures 29–31 represent the results for the 3.2-, 6-, and 12-mm tile thicknesses, respectively. As seen in figure 29, abrading the specimens caused the failure load to decrease, as well as the experimental scatter, compared to the as-received samples.

For example, the failure load for the as-received samples tested with the 0.5-in steel ball was 1.608 ± 0.590 kN, whereas the samples abraded on the bottom (tension) surface, and also tested with the 0.5-in steel ball, had a failure load of 0.445 ± 0.049 kN.

Thus, the abrasion treatment was effective in producing a more uniform flaw size distribution. However, the flaws that were introduced were much larger than the flaws on the as-received glasses, causing much lower failure loads.

However, this is okay, since what is being sought are any differences in failure load due to variations in ball diameter and tile thickness, while keeping flaw size more-or-less constant. All tiles failed from back-face radial cracks initiated by the equibiaxial tensile stress field.

Figure 29 shows that the failure loads did not change with ball diameter in the 0.0625- to 0.5-in range, despite the fact that ring-cone cracks initiated for the tests conducted with the 0.0625- and 0.25-in-diameter balls. This indicates that tile failure was still controlled by the back-face radial crack tension failures, i.e., the ring-cone cracks played little, if any, role in the overall failure of the tiles.

For those tests where no ring-cone cracks initiated, failure stresses were calculated according to (59):

$$\sigma_{\max} = \frac{3P(1+\nu)}{4\pi t^2} \left[1 + 2 \ln \frac{a}{b} + \frac{(1-\nu)}{(1+\nu)} \left\{ 1 - \frac{b^2}{2a^2} \right\} \frac{a^2}{R^2} \right], \quad (1)$$

with σ_{\max} failure stress, P failure load, ν Poisson's ratio of specimen, t specimen thickness, a support radius, b radius of uniform stress ($\sim t/3$), and R radius of disk (for square specimen $R = x/2$; x = edge length of tile). This equation assumes equibiaxial stress conditions, where the radial and tangential stresses are assumed equal.

Table 8. Starphire glass failure test results.^a

Quantity of Tiles Evaluated	No. Tiles Tested	Steel Ball Diameter (in)	Failure Load (kN)	Failure Stress (MPa)	Ring/Cone Initiation Load (N)	Macro Conoid	Backface Radial Cracks	T (°C)	Relative Humidity (%)
3.2-mm-Thick Tiles									
As-received top and bottom	12	0.5	1.608 ± 0.590	226 ± 83	No	No	Yes	22	49
As-received top; abraded bottom	12	0.5	0.445 ± 0.049	63 ± 7	No	No	Yes	18	57
Abraded top and bottom	12	0.0625	0.452 ± 0.061	—	66 ± 12	No	Yes	22	47
Abraded top and bottom	10	0.25	0.476 ± 0.054	—	214 ± 42	No	Yes	22	48
Abraded top and bottom	11	0.5	0.457 ± 0.051	64 ± 7	No	No	Yes	22	48
6-mm-Thick Tiles									
Abraded top and bottom	12	0.0625	1.580 ± 0.184	—	90 ± 29	Yes (40%)	Yes ^b	21	24
Abraded top and bottom	12	0.125	1.613 ± 0.163	—	86 ± 13	Yes (60%)	Yes	22	46
Abraded top and bottom	8	0.25	1.595 ± 0.173	—	113 ± 13	No	Yes	20	37
Abraded top and bottom	12	0.5	1.674 ± 0.169	—	237 ± 27	No	Yes	22	48
Abraded top and bottom	10	1.5	1.654 ± 0.207	97 ± 12	No	No	Yes	22	47
12-mm-Thick Tiles									
Abraded top and bottom	12	0.25	9.982 ± 1.029	—	139 ± 50	Yes (100%)	Yes ^c	22	49
Abraded top and bottom	12	0.5	10.003 ± 0.696	—	336 ± 85	Yes (100%)	Yes ^d	22	42
Abraded top and bottom	12	0.75	10.529 ± 1.317	—	454 ± 124	Yes (100%)	Yes ^d	21	25
Abraded top and bottom	12	1.5	10.124 ± 0.75	—	610 ± 105	Yes (100%)	Yes	23	45

Note: Parentheses indicate percentage of tests displaying that behavior.

^aValues in table are average ±1 standard deviation.

^bSurface spalls formed as well (30% of tests).

^cSurface spalls and surface radials formed as well (100% of tests).

^dSurface radials formed as well (100% of tests).

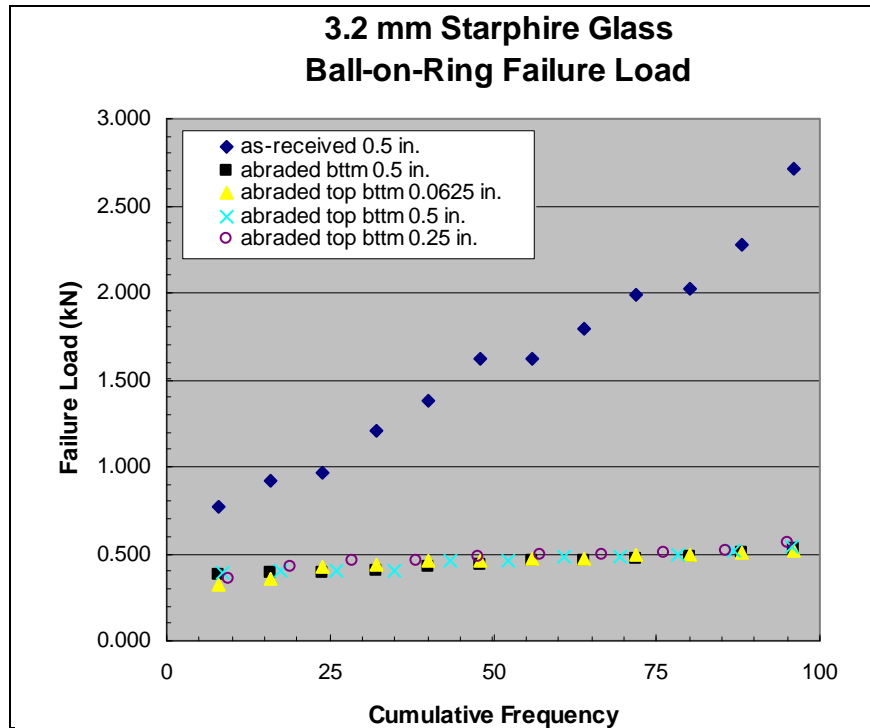


Figure 29. Failure load for the 3.2-mm-thick Starphire glass tiles loaded with steel balls of different diameter.

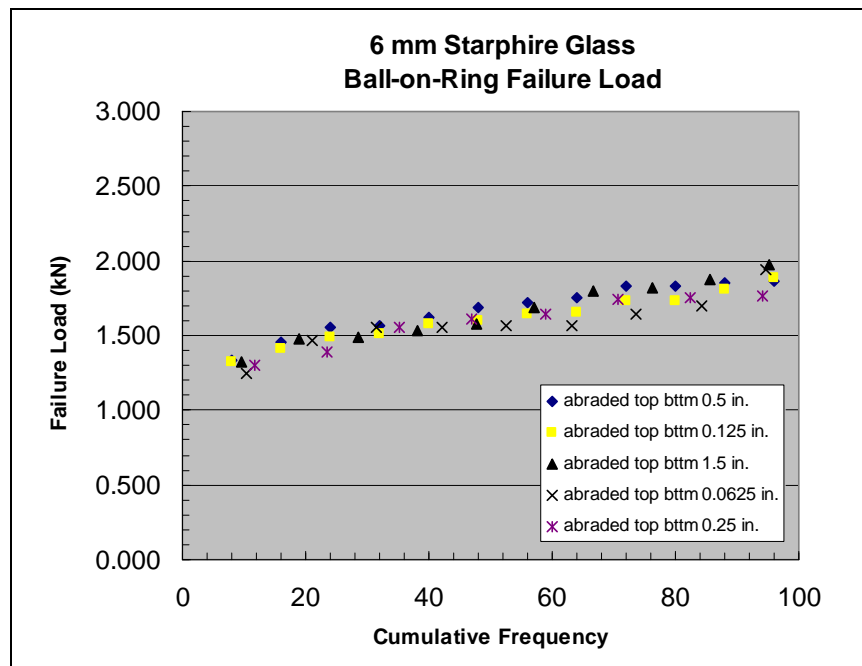


Figure 30. Failure load for the 6-mm-thick Starphire glass tiles loaded with steel balls of different diameter.

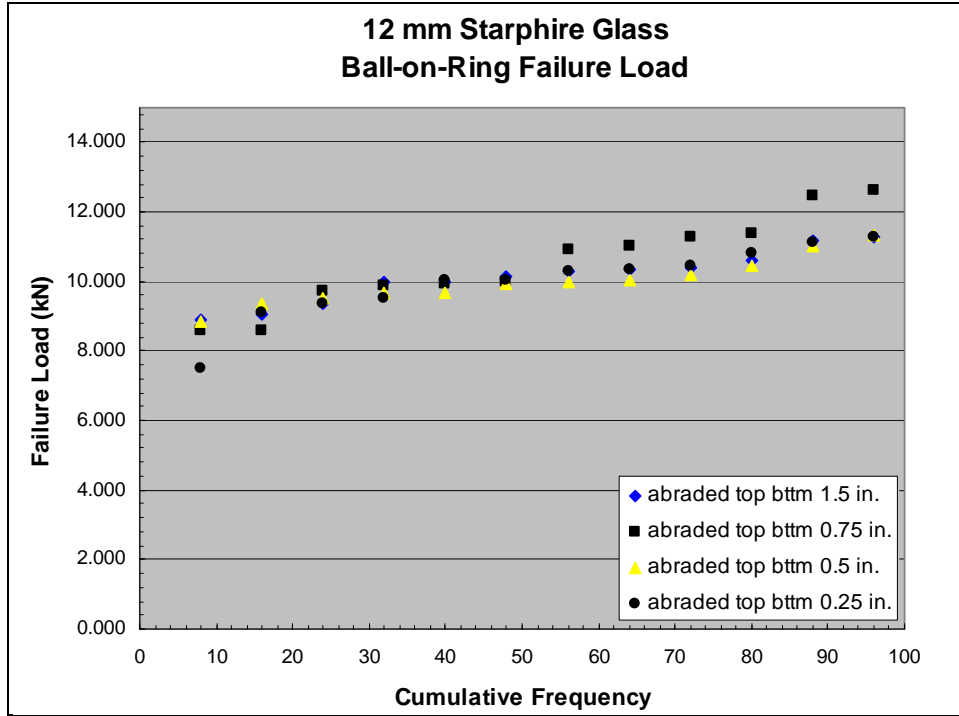


Figure 31. Failure load for 12-mm-thick Starphire glass tiles loaded with steel balls of different diameter.

Note how the ball size does not enter the equation. As-received specimens had failure stresses of 226 ± 83 MPa compared to 63 ± 7 MPa for abraded specimens.

Figure 32 illustrates several failed 3.2-mm Starphire tiles tested with balls of various diameter. Back-face radial cracking caused the failures. All tiles shown were abraded on the top and bottom surfaces, with the exception of the lower-left tile, where only the bottom surface was abraded. Figure 33 is an as-received tile failed by loading with a 0.5-in ball. Note how there are many more cracks compared to the abraded specimens, indicating a much greater stress (energy) at the time of failure, consistent with the higher failure loads for these tiles (see table 8).

4.2.2.2 6-mm Tiles. Compared to the 3.2-mm tiles, ring-cone cracks initiated using the 0.5-in-diameter steel ball indenter (and all other smaller-diameter indenters as well). However, macro conoid cracks formed in 40% and 60% of the tests made with the 0.0625- and 0.125-in balls. The macro conoids are thought to be the extensions of the small ring-cone cracks that form early on loading but which are then propagated through the specimen thickness at the time of failure.

The reason for the dependence of macro conoid formation on ball diameter is not entirely understood, particularly since the size to which cone cracks grow is not governed by indenter diameter, but by material properties and indentation load (22):

$$\frac{P^2}{R^3} = \frac{2E\gamma_f}{\kappa(\nu)}, \quad (2)$$



Figure 32. Several failed 3.2-mm Starphire tiles. The star-like fracture patterns are typical of biaxial flexural testing. Top row, left to right: 0.125-, 0.25-, and 0.5-in ball. Bottom row, left to right: 0.5-in ball and only bottom surface abraded, 0.0625-in ball. Tiles are $4 \times 4 \text{ in}^2$.



Figure 33. As-received 3.2-mm Starphire tile loaded to failure with 0.5-in steel ball. Tile is $4 \times 4 \text{ in}^2$.

with P indentation load, R radius of base of cone crack, E Young's modulus, γ_f fracture surface energy, and $\kappa(\nu)$ a constant dependent on Poisson's ratio and equal to 2.75×10^{-3} for $\nu = 0.25$. Poisson's ratio for Starphire glass is ~ 0.22 .

However, one possible explanation is that for these small-diameter indenters (0.0625 and 0.125 in), the stress level in the glass is approaching the yield stress, and this alters the trajectory of the initially small cone crack, causing it to propagate more steeply compared to conditions of purely elastic contact for more blunt indenters.

In figure 34, the mean contact stress (not the tensile fracture stress) at the moment of ring-crack initiation is plotted as a function of ball diameter for the tin side of Starphire glass. The fracture stress is lower since the ring cracks form just outside the contact edge. These data were obtained from separate experiments in which an unabraded 12-mm-thick Starphire tile was rigidly supported. For the 0.125-in-diameter indenter, the mean stress is about 4.5 GPa, which is approaching the yield stress based on Vickers hardness measurements (see table 4).

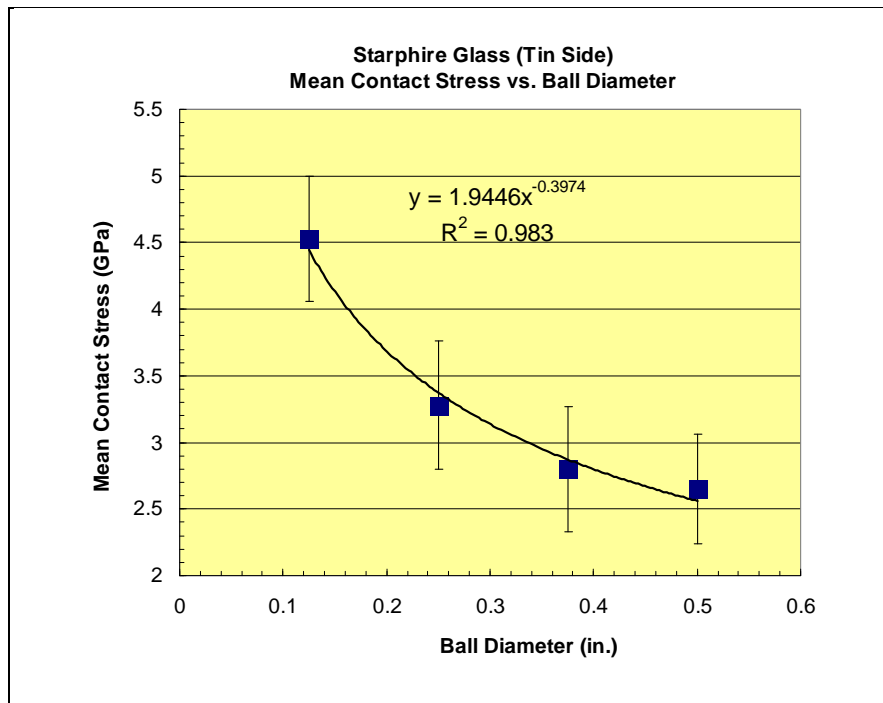


Figure 34. Mean contact stress at the initiation load for ring-cone cracks as a function of the ball diameter for the tin side of Starphire glass. Data for an unabraded tile.

When the power-law curve fit is used (see figure 34), the mean contact stress is estimated to be ~ 5.8 GPa for the 0.0625-in-diameter indenter. This value is higher than the Vickers hardness and approaches the value of yield stress found from the instrumented tests conducted with the 500- μm -diameter diamond sphere (see section 4.1.2).

Thus, it is possible that yielding is taking place around the same time the ring-cone cracks are forming. The yielding may cause the cone cracks to propagate more steeply and penetrate the tensile bending region, driving the small conoid into a large conoid that pops out on the tension side of the specimen. For the more blunt indenters (0.25 in and larger), the contact stress never reaches high enough to cause yielding before failure, hence the ring-cone cracks that initiate are not as steep and no macro conoids form.

Although the mean contact stresses shown in figure 34 are well above the yield stress for the steel balls (~2 GPa, see section 4.2), no permanent deformation (dimpling) of the balls was seen, although some scratches necessitated rotating or changing the balls periodically.

Three of the tiles tested with the 0.0625-in ball did not fail, but rather severe surface spalling and comminution occurred, causing the ball to be completely buried in the sample, up to the indenter holder. These tests were stopped before the tile failed.

It is very important to point out that the formation of the macro conoids did not affect the failure loads above the normal experimental variability seen (see table 8). For example, with the 0.0625-in ball, one tile that did not form a macro conoid failed at 1.550 kN, whereas another tile that did form a macro conoid failed at 1.569 kN. This means the back-face radial cracks are still dominating the overall failure behavior.

Figure 35 (a) and (b) illustrate these two failed 6-mm tiles mentioned previously, without and with macro conoid formation, respectively. Cursory fractography revealed that the skirt of the macro conoid was discontinuous where it intersected the back-face radial cracks, indicating the radial cracks had a slight head start during failure. Much more fractography needs to be done on all tiles to confirm these and other observations.

4.2.2.3 12-mm Tiles. All of the 12-mm-thick tiles formed macro conoid cracks for all ball diameters. An example of a macro conoid formation is shown in figure 36 for a tile indented with a 0.75-in-diameter steel ball. All of the macro conoids that formed were substantially larger than those found in the 6-mm tiles.

The obvious conclusion is that tile thickness is a key variable in influencing the macro conoid formation. A possible explanation is that the cone cracks are able to grow larger in the 12-mm tiles, relative to the tile thickness, due to less bending. Greater bending, such as in the 6-mm tiles, would presumably reduce cone crack growth via increased surface compression.

Less bending would allow the cone crack to propagate relatively further into the specimen for a given load, compared to the 6-mm tiles. This larger cone crack can then be thrust through once the back-face radial cracks start the structural failure process.

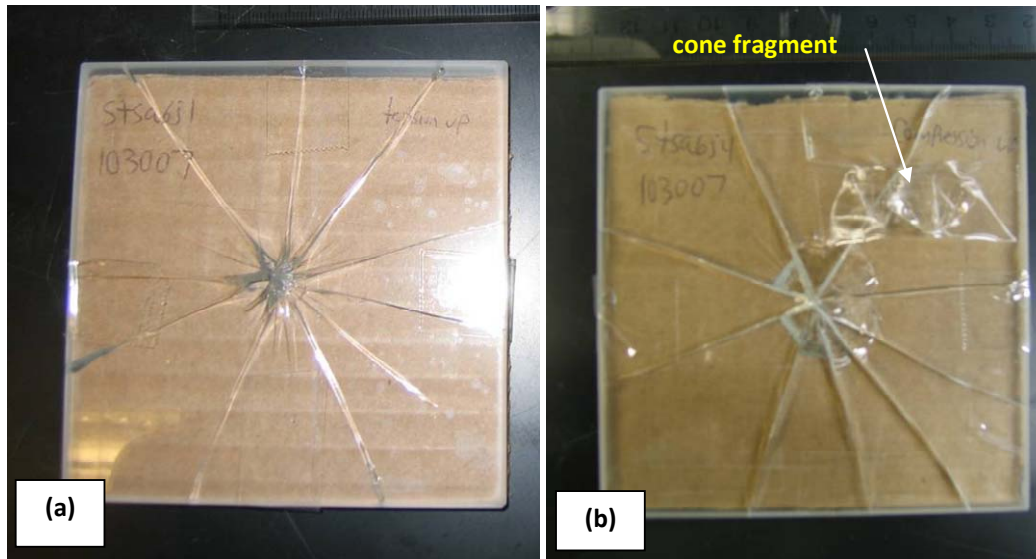


Figure 35. Failed 6-mm Starphire tiles that formed no macro conoid (a) and that did form a macro conoid (b). Tension side faces up (a) and compression side faces up (b). Steel ball diameter 0.0625 in. Tiles are 4×4 in².

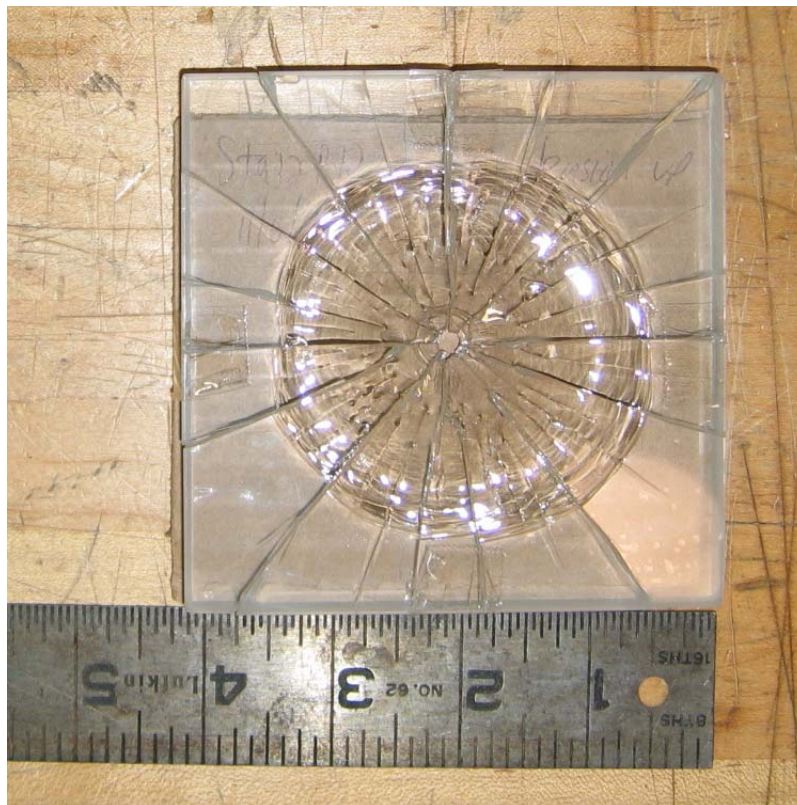


Figure 36. Failed 12-mm Starphire tile loaded with a 0.75-in-diameter steel ball. The tension side, illustrating the large crater formed from the macro conoid, faces up. The chipped away pieces are not shown.

The fact that large segments of material were removed where the cone crack intersected the rear surface tends to confirm that the back-face radial cracks were present before the cone crack reached the rear surface. This means the “macro conoid” was probably propagating as separate segments, at least during the latter stages of its growth.

More fractography needs to be done to clarify these and other issues. In addition, by the time the macro conoid reached the rear surface, it was nearly parallel to the tile surface, as seen in figure 36. This is believed to be caused by the tile bending.

Regardless of the timing sequence, the formation of a macro conoid will drastically reduce the structure’s ability to withstand further impacts, since a major portion of the target will either be completely missing or weakly held in place.

In addition to the macro conoids and back-face radial cracks that formed, surface radial cracks also formed for tests performed with the 0.25-, 0.5-, and 0.75-in ball diameters. These cracks were small and may not have played a major role in the failures. However, the presence of these cracks possibly suggests inelastic deformation occurring, since radial cracks in glass around Vickers indentations are thought to arise from inelastic deformation processes, as discussed in detail by Lawn and Wilshaw (22).

For the 0.25-in indenter, surface spalls formed in all tiles prior to failure. These spalls appeared to consist of both lateral-type cracks and comminuted material. The small diameter of the indenter appeared to generate stresses that would fail material in a localized region before the tile failed from the back-face and macro conoid cracks.

An indentation sequence showing the initiation of a ring-cone crack and the spall failure is shown in figure 37 for a test made with the 0.25-in-diameter steel ball. In frame (d), the spall failure is visible, and the tile failed completely and catastrophically shortly after.

Figure 38 shows the average failure load for the abraded top and bottom specimens as a function of tile thickness. It is apparent that the failure load increases as the square or exponential of the tile thickness.

Finally, the experimental variability in fracture loads was considerably greater compared to the 3.2- and 6-mm tiles (see table 8). Reasons for this are not entirely known, but perhaps the macro conoids are influencing the overall structural failure behavior to a greater extent compared to the 6-mm tiles.

It is important to note that in all tests, and for all tile thicknesses, i.e., 3.2, 6, and 12 mm, the ring cracks that initiated did so stably, i.e., no abrupt pop-in was observed. This is due to the large starting flaw sizes introduced by the abrasion treatment, which stabilizes the initiation process.

Part of a ring crack would initiate and grow downward while slowly spreading around the rest of the contact, as shown in figure 37 (a). When the ring was complete, further load increases resulted in just growth of the cone crack.

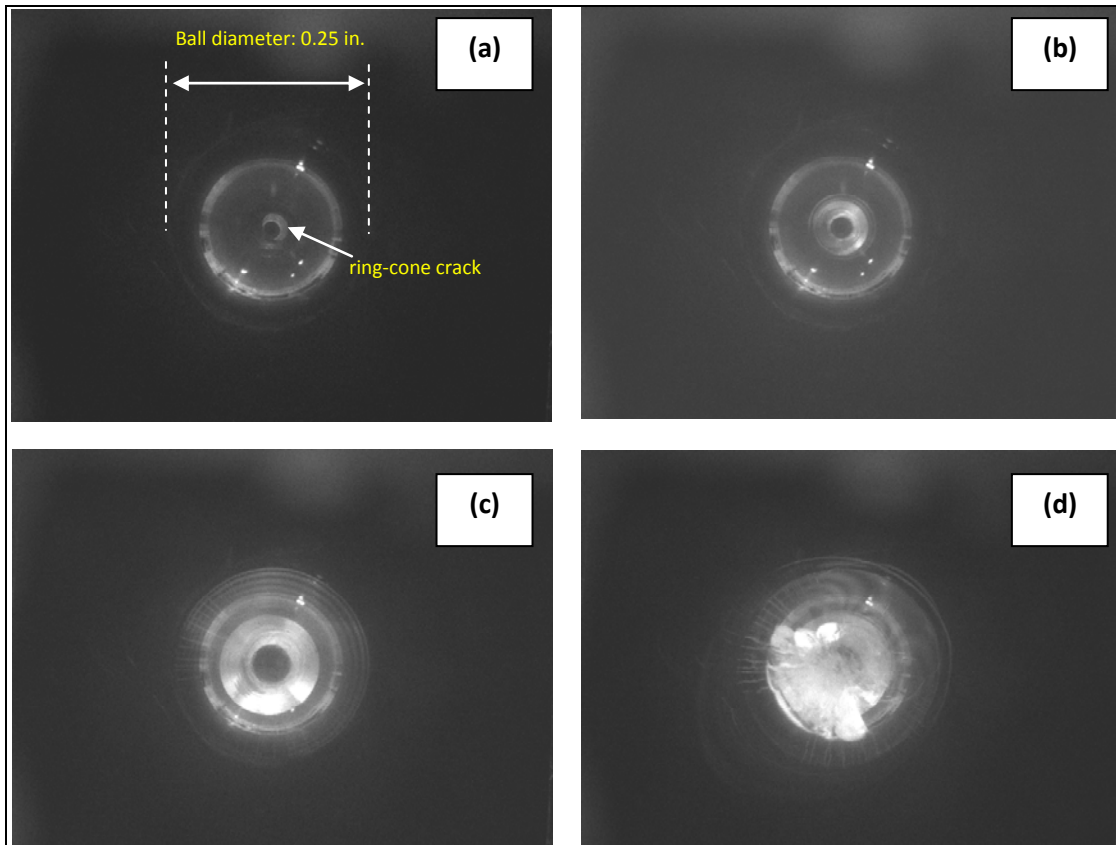


Figure 37. A sequence of frames illustrating the formation and growth of the ring-cone crack (a–c), and the initiation of the spall failure (d) in the 12-mm Starphire tile (tin side) contacted with the 0.25-in-diameter steel ball. Load increases from a to d.

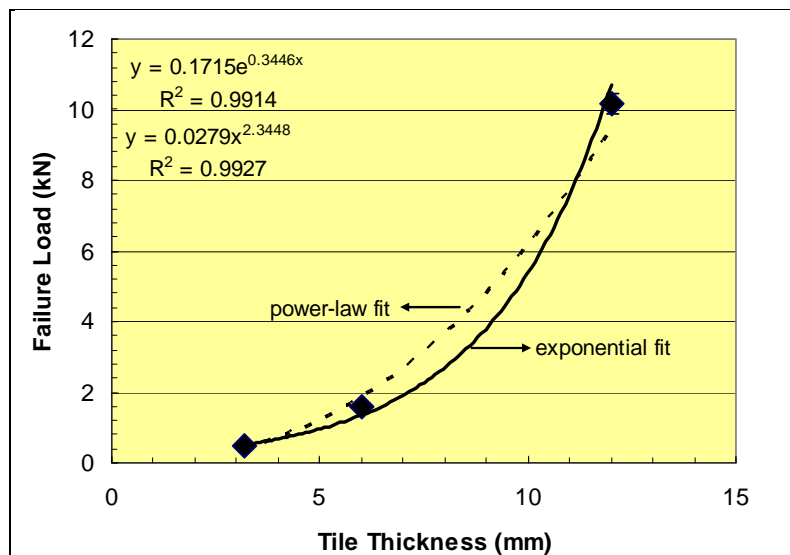


Figure 38. Average failure load as a function of tile thickness. Two different curve fits of the data show the exponential or power-law dependence on tile thickness.

4.2.3 Flaw Size Estimates

An attempt is made to calculate the flaw sizes responsible for failure for the as-received and abraded test specimens. Using the failure stress for the as-received samples, i.e., 226 MPa, and the fracture mechanics expression for a surface flaw in uniform tension, i.e.,

$$K_{Ic} = 1.12\sigma_f\sqrt{\pi c} \quad , \quad (3)$$

one can solve for the crack depth, c . When a value of $0.70 \text{ MPa}\sqrt{\text{m}}$ for Starphire glass is used, which is reasonable, the flaw size is $c \approx 2.4 \text{ }\mu\text{m}$. For the abraded specimens with fracture stress of 64 MPa, the flaw depth is calculated to be $c \approx 30 \text{ }\mu\text{m}$.

If to a first approximation the flaws are assumed nearly semi-circular, this depth would correspond to a surface flaw length of $\sim 60 \text{ }\mu\text{m}$, which approaches the average 220-grit SiC particle size of $\sim 63 \text{ }\mu\text{m}$.

4.3 Other Experiments

Figure 39 shows the ring crack stress as a function of ball diameter for the tin sides of both Starphire and Borofloat glasses. This stress was calculated using equation 4 (see the appendix), using the measured ring-crack radii obtained from posttest microscopy. The fracture stress decreases with increasing ball size in accord with the experimental results of Tillett (25).

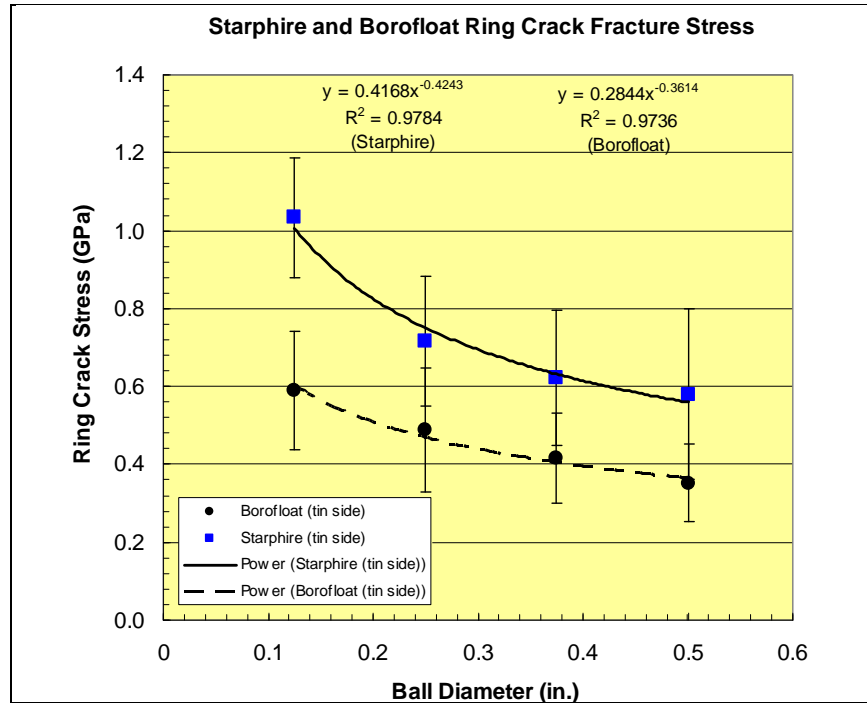


Figure 39. Ring crack stress as a function of ball diameter for the tin sides of unabraded Starphire and Borofloat glasses.

This phenomenon is a consequence of the highly inhomogeneous stress field that exists around small-sized indenters, causing the stress at fracture to increase with decreasing ball size (40). For larger indenters, the stress field is more uniform over the flaw, which gives rise to a nearly constant fracture stress.

It is experimentally observed that the critical load for ring crack formation is proportional to the indenter radius, r , for small-sized indenters, i.e., $P_c \propto r$, a phenomenon known as Auerbach's law (40). For larger indenters, it is observed that $P_c \propto r^2$. Figure 40 illustrates this for the Starphire and Borofloat glasses.

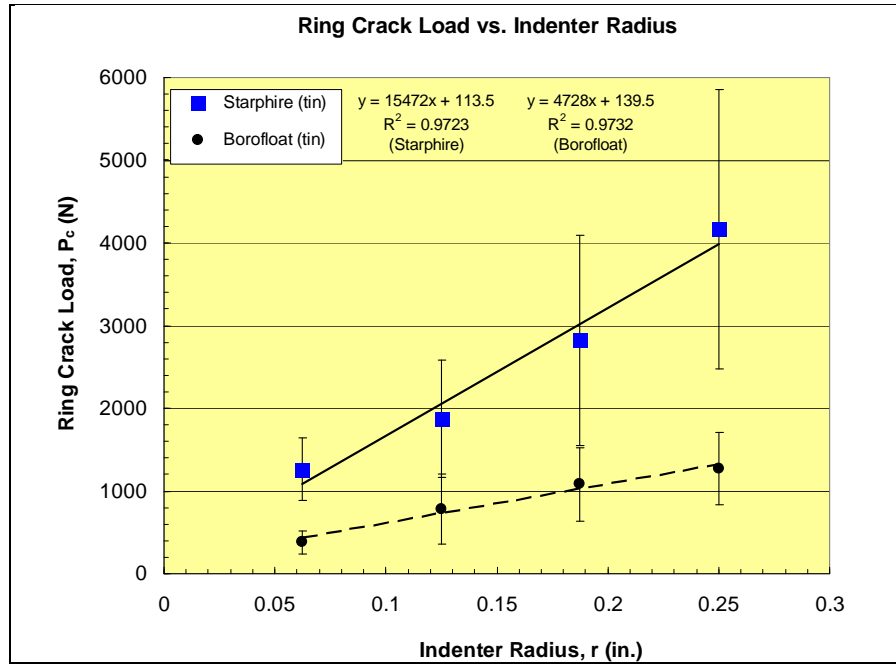


Figure 40. Ring crack load as a function of ball diameter for the tin sides of unabraded Starphire and Borofloat glasses.

It is important to point out here that the initiation of the cone cracks was simultaneous with the initiation of the ring cracks, i.e., an unstable crack system was formed from the start.

The maximum Hertzian tensile stress can be expressed as (18):

$$\sigma_m = \left(\frac{1-2\nu}{2} \right) \left(\frac{3E}{4k} \right)^{2/3} \left(\frac{P}{\pi r^2} \right)^{1/3} . \quad (4)$$

This is analogous to equation 4 (the appendix) with $\rho = a$, i.e., at the contact periphery and with the last two terms on the right side of equation 4 substituted in place of p_o .

At fracture, $\sigma_m = \sigma_f$ and $P = P_c$. Since for large indenters $P_c \propto r^2$, equation 4 yields $\sigma_m = \text{constant}$ and independent of indenter size. This holds for a given flaw size. In this large indenter region, the fracture stress is dependent on flaw size, i.e., $P_c \propto c_f^{-3/2}$ (40). That is, P_c decreases with increasing flaw size in this region.

For the small indenter (Auerbach) region where $P_c \propto r$, equation 4 yields $\sigma_m \propto r^{-1/3}$. That is, the fracture stress is expected to decrease with increasing ball size raised to the negative one-third power. In this region the fracture stress is found to be relatively independent of flaw size (40).

The data in figure 39 were fit with an inverse power law, and the exponents for the Starphire and Borofloat glasses were -0.42 and -0.36 , respectively. These values are close to the theoretical value of -0.33 . Of course, plotting the data as stress vs. ball diameter instead of stress vs. ball radius has no effect on the value of the exponents.

If larger-diameter ball indenters were used, the fracture stress is expected to decrease to a more-or-less constant value, similar to what Tillett (25) observed in her experiments.

It is worthwhile to estimate the flaw size from the 0.5-in ring crack stress for the Starphire glass in figure 39. Taking the fracture stress as ~ 600 MPa (0.6 GPa) from the graph and using equation 4 with K_{Ic} of $0.70 \text{ MPa}\sqrt{\text{m}}$ yields $c \sim 0.35 \text{ }\mu\text{m}$. This is smaller than the flaw size from the equibiaxial flexure tests ($c \sim 2.4 \text{ }\mu\text{m}$).

However, the ring crack stress has not reached its lower plateau value, and a larger value of flaw size would be calculated if the failure stress from larger ball diameters had been used.

5. Summary and Conclusions

In the current work, IIT was used to study the deformation and fracture behavior of three different glass compositions and AlON to localized contact from a 500- μm -diameter diamond spherical indenter.

In addition, structural failure experiments were conducted on Starphire glass tiles in which large macro conoid cracks were initiated in the thicker specimens. This behavior mimics the large conoid cracks sometimes seen in ballistic tests.

Additional Hertzian fracture tests for measuring ring crack loads and stress were carried out on Starphire and Borofloat glass tiles.

Several conclusions can be made in connection with the work performed here:

1. IIT can be used to easily measure yield stress at room temperature in glass and ceramic materials, and study localized fracture behavior in a controlled manner. These parameters

should be compared to the materials' actual ballistic performance for the sake of determining any correlations.

2. Large macro conoid cracks, spalls, back-face radial cracks, and smaller surface-localized radial cracks can be formed under quasi-static test conditions in tiles of substantial thickness when subjected to sufficiently high loads with spherical indenters of appropriate size.

Failure resulting from such a combination of damage modes may possibly be relevant to ballistic performance. Hence, this type of testing should at least be considered, in addition to the IIT testing, for the screening of candidate materials.

3. The macro conoid cracks formed in the 12-mm-thick tiles were nearly parallel to the tile by the time they reached and intersected the rear surface. This is believed to be a result of the bending of the tile, which "flattens out" the cone crack trajectory. This may be useful behavior to exploit.

6. Future Work

A more in-depth fractographic analysis of the failed tiles would be useful, including measurements of the macro conoid diameter. This would help clarify issues relating to the sequence of the fracture processes in the case of the thicker tiles.

In addition, the morphologies of the macro conoids should be examined, with emphasis on the angles of these cracks. One way to do this is to make a replica of the cone crack fracture surface, possibly using heat-shrink tape, which would yield a positive replica of the cone crack that could be easily removed and analyzed. In addition, exploiting tile bending as a way to control the angle of the cone crack may be beneficial.

Additional work should be done to study the influence of indenter diameter and indenter material on the yield stress and fracture behavior.

7. References

1. Shockey, D. A.; Marchand, A. H.; Skaggs, S. R.; Cort, G. E.; Burkett, M. W.; Parker, R. Failure Phenomenology of Confined Targets and Impacting Rods. In *Ceramic Armor Materials by Design*; McCauley, J. W., Crowsoon, A., Gooch, W. A., Jr., Rajendran, A. M., Bless, S. J., Logan, K. V., Normandia, M., Wax, S., Eds.; The American Ceramic Society: Westerville, OH, 2002; pp 385–402.
2. Sherman, D.; Ben-Shushan, T. Quasi-Static Impact Damage in Confined Ceramic Tiles. *Int. J. Impact Eng.* **1998**, *21* (4), 245–265.
3. Sherman, D. Impact Failure Mechanisms in Alumina Tiles on Finite Thickness Support and the Effect of Confinement. *Int. J. Impact Eng.* **2000**, *24*, 313–328.
4. Hauver, G.; Rapacki, E. J., Jr.; Netherwood, P. H.; Benck, R. F. *Interface Defeat of Long-Rod Projectiles by Ceramic Armor*; ARL-TR-3590; U.S. Army Research Laboratory: Aberdeen Proving Ground, MD, September 2005.
5. Wilkins, M. L.; Cline, C. F.; Honodel, C. A. *Light Armor*; Lawrence Radiation Laboratory, University of California: Livermore, CA, 1969.
6. Shockey, D. A.; Rowcliffe, D. J.; Dao, K. C.; Seaman, L. Particle Impact Damage in Silicon Nitride. *J. Am. Ceram. Soc.* **1990**, *73* (6), 1613–1619.
7. Kim, D. K.; Lee, C. S.; Kim, Y. G.; Kim, C. W.; Chang, S. N. Dynamic Indentation Damage of Ceramics. In *Ceramic Armor Materials By Design*; McCauley, J. W., Crowsoon, A., Gooch, W. A., Jr., Rajendran, A. M., Bless, S. J., Logan, K. V., Normandia, M., Wax, S., Eds.; The American Ceramic Society: Westerville, OH, 2002; pp 261–268.
8. Evans, A. G.; Gulden, M. E. Impact Damage in Brittle Materials in the Elastic-Plastic Response Regime. *Proc. R. Soc. London A* **1978**, *361*, 343–365.
9. Akimune, Y.; Katano, Y.; Matoba, K. Spherical-Impact Damage and Strength Degradation in Silicon Carbide Whisker/Silicon Nitride Composites. *J. Am. Ceram. Soc.* **1989**, *72* (5), 791–798.
10. Akimune, Y. Impact Damage and Strength Degradation in a Silicon Carbide Reinforced Silicon Nitride Composite. *J. Am. Ceram. Soc.* **1990**, *73* (10), 3019–3025.
11. LaSalvia, J. C.; Normandia, M. J.; Miller, H. T.; MacKenzie, D. E. Sphere Impact Induced Damage in Ceramics: I. Armor-Grade SiC and TiB₂. *Ceram. Eng. Sci. Proc.* **2005**, *26* (7), 171–181.

12. LaSalvia, J. C.; Normandia, M. J.; Miller, H. T.; MacKenzie, D. E. Sphere Impact Induced Damage in Ceramics: II. Armor-Grade B₄C and WC. *Ceram. Eng. Sci Proc.* **2005**, 26 (7), 183–192.
13. LaSalvia, J. C.; Normandia, M. J.; Miller, H. T.; MacKenzie, D. E. Sphere Impact Induced Damage in Ceramics: III. Analysis. *Ceram. Eng. Sci Proc.* **2005**, 26 (7), 193–202.
14. Kirchner, H. P.; Larchuk, T. J. Comparisons of Static and Impact Loading Damage in Zinc Sulfide. *J. Am. Ceram. Soc.* **1982**, 65 (10), 506–510.
15. Chaudhri, M. M.; Kurkjian, C. R. Impact of Small Steel Spheres on the Surfaces of ‘Normal’ and ‘Anomalous’ Glasses. *J. Am. Ceram. Soc.* **1986**, 69 (5), 404–409.
16. Wiederhorn, S. M.; Lawn, B. R. Strength Degradation of Glass Resulting From Impact With Spheres. *J. Am. Ceram. Soc.* **1977**, 60 (9–10), 451–458.
17. Chaudhri, M. M. High-Speed Photographic Investigations of the Dynamic Localized Loading of Some Oxide Glasses. In *Strength of Inorganic Glass*; Kurkjian, C. R., Ed.; Plenum Press: New York, 1985; 87–114.
18. Lawn, B. R. Indentation of Ceramics With Spheres: A Century After Hertz. *J. Am. Ceram. Soc.* **1998**, 81 (8), 1977–1994.
19. Padture, N.; Lawn, B. R. Contact Fatigue of a Silicon Carbide With a Heterogeneous Grain Structure. *J. Am. Ceram. Soc.* **1995**, 78 (6), 1431–1438.
20. Padture, N.; Lawn, B. R. Toughness Properties of a Silicon Carbide With an *in Situ* Induced Heterogeneous Grain Structure. *J. Am. Ceram. Soc.* **1994**, 77 (10), 2518–2522.
21. Lawn, B. R.; Lee, S. K.; Peterson, I. M.; Wuttiaphan, S. Model of Strength Degradation From Hertzian Contact Damage in Tough Ceramics. *J. Am. Ceram. Soc.* **1998**, 81 (6), 1509–1520.
22. Lawn, B. R.; Wilshaw, R. Review Indentation Fracture: Principles and Applications. *J. Mater. Sci.* **1975**, 10, 1049–1081.
23. Wilshaw, T. R. The Hertzian Fracture Test. *Phys. D. Appl. Phys.* **1971**, 4, 1567–1581.
24. Roesler, F. C. Brittle Fractures Near Equilibrium. *Proceedings of Phys. Soc. B* **1956**, 69, 981–992.
25. Tillett, J. P. A. Fracture of Glass by Spherical Indenters. *Proc. Phys. Soc. B* **1955**, 69, 47–54.
26. Benbow, J. J. Cone Cracks in Fused Silica. *Proc. Phys. Soc. B* **1959**, 75, 697–699.
27. Wilkins, M. L.; Cline, C. F.; Honodel, C. A. *Light Armor*; Lawrence Radiation Laboratory, University of California: Livermore, CA, 1969.

28. Sternberg, J. Material Properties Determining the Resistance of Ceramics to High Velocity Penetration. *J. Appl. Phys.* **1989**, 65 (9), 3417–3424.
29. Flinders, M.; Ray, D.; Anderson, A.; Cutler, R. A. High-Toughness Silicon Carbide as Armor. *J. Am. Ceram. Soc.* **2005**, 88 (8), 2217–2226.
30. Milman, Yu. V.; Chugunova, S. I. Mechanical Properties, Indentation and Dynamic Yield Stress of Ceramic Targets. *Int. J. Impact Eng* **1999**, 23, 629–638.
31. Milman, Yu. V.; Chugunova, S. I.; Timofeeva, I. I. The Resistance of Silicon Carbide to Static and Impact Loading. *Int. J. Impact Eng* **2001**, 26, 533–542.
32. Vichniecki, D.; Blumenthal, W.; Slavin, M.; Tracy, C.; Skeeel, H. Armor Ceramics. Presented at the Third Tacom Armor Coordinating Conference, Monterey, CA, 17–19 February 1987.
33. Hertz, H. *J. Reine Angew. Math.* **1881**, 92, (156); *Verhandlungen des Vereins zur Beförderung des Gewerbe Fleisses* **1882**, 61, (449). Reprinted in English in Hertz's Miscellaneous Papers, Macmillan: London, 1896; Chapters 5, 6.
34. Frank, F. C.; Lawn, B. R. On the Theory of Hertzian Fracture. *Proc. R. Soc. A* **1967**, 299, 291–306.
35. Chen, S. Y.; Farris, T. N.; Chandrasekar, S. Contact Mechanics of Hertzian Cone Cracking. *Int. J. Solids Structures* **1995**, 32 (3–4), 329–340.
36. Zeng, K.; Breder, K.; Rowcliffe, D. J. The Hertzian Stress Field and Formation of Cone Cracks-I. Theoretical Approach. *Acta Metall. Mater.* **1992**, 40 (10), 2595–2600.
37. Kocer, C.; Collins, R. E. Angle of Hertzian Cone Cracks. *J. Am. Ceram. Soc.* **1998**, 81 (7), 1736–1742.
38. Mouginot, R.; Maugis, D. Fracture Indentation Beneath Flat and Spherical Punches. *J. Mater. Sci.* **1985**, 20, 4354–4376.
39. Fischer-Cripps, A. C. Predicting Hertzian Fracture. *J. Mater. Sci.* **1997**, 32, 1277–1285.
40. Langitan, F. B.; Lawn, B. R. Hertzian Fracture Experiments on Abraded Glass Surfaces as Definitive Evidence for an Energy Balance Explanation of Auerbach's Law. *J. Appl. Phys.* **1969**, 40 (10), 4009–4017.
41. Langitan, F. B.; Lawn, B. R. Effect of a Reactive Environment on the Hertzian Strength of Brittle Solids. *J. Appl. Phys.* **1970**, 41 (8), 3357–3365.
42. Mikosza, A. G.; Lawn, B. R. Section-and-Etch Study of Hertzian Fracture Mechanics. *J. Appl. Phys.* **1971**, 42 (13), 5540–5545.
43. Warren, R. Measurement of the Fracture Properties of Brittle Solids by Hertzian Indentation. *Acta Metall.* **1978**, 26, 1759–1769.

44. Lawn, B. R.; Wilshaw, T. R.; Hartley, N. E. W. A Computer Simulation Study of Hertzian Cone Crack Growth. *Int. J. Fracture* **1974**, *10* (1), 1–16.
45. Fischer-Cripps, A. C.; Collins, R. E. The Probability of Hertzian Fracture. *J. Mater. Sci.* **1994**, *29* (8), 2216–2230.
46. Fett, T.; Rizzi, G.; Diegele, E. Weight Functions for Cone Cracks. *Eng. Fract. Mech.* **2004**, *71*, 2551–2560.
47. Swain, M. V.; Hagan, J. T. Indentation Plasticity and the Ensuing Fracture of Glass. *J. Phys. D: Appl. Phys.* **1976**, *9*, 2201–2214.
48. Hagan, J. T.; Swain, M. V. The Origin of Median and Lateral Cracks Around Plastic Indents in Brittle Materials. *J. Phys. D: Appl. Phys.* **1978**, *11*, 2091–2102.
49. Lawn, B. R.; Dabbs, T. P.; Fairbanks, C. J. Kinetics of Shear-Activated Indentation Crack Initiation in Soda-Lime Glass. *J. Mater. Sci.* **1983**, *18* (9), 2785–2797.
50. Haranoh, T.; Ishikawa, H.; Shinkai, N.; Mizuhashi, M. Crack Evolution in Vickers Indentation for Soda-Lime-Silica Glass. *J. Mater. Sci.* **1982**, *17* (5), 1493–1500.
51. Lardner, T. J.; Ritter, J. E.; Zhu, G. Q. Spherical Indentation and Fracture of Glass Plates. *J. Am. Ceram. Soc.* **1997**, *80* (7), 1851–1862.
52. Swab, J. J.; Gilde, G. A.; Patel, P. J.; McCauley, J. W. Fracture Analysis of Transparent Armor Ceramics. In *Proceedings of the Fourth Alfred Conference on the Fractography of Glasses and Ceramics*; American Ceramic Society: Westerville, OH, 2001; pp 489–508.
53. Kingery, W. D.; Bowen, H. K.; Uhlman, D. R. *Introduction to Ceramics*, 2nd ed.; Wiley & Sons: New York, 1976; Chapter 3.
54. Graham, E. K.; Munly, W. C.; McCauley, J. W.; Corbin, N. D. Elastic Properties of Polycrystalline Aluminum Oxynitride Spinel and Their Dependence on Pressure, Temperature, and Composition. *J. Am. Ceram. Soc.* **1988**, *71* (10), 807–812.
55. Chandler, H. *Hardness Testing*; ASM International: Materials Park, OH, 1999.
56. Tabor, D. *The Hardness of Metals*; Oxford University Press: Oxford, U.K., 1951.
57. Hockey, B. J. Plastic Deformation of Aluminum Oxide by Indentation and Abrasion. *J. Am. Ceram. Soc.* **1971**, *54* (5), 223–231.
58. Hertzberg, R. W. *Deformation and Fracture Mechanics of Engineering Materials*, 2nd ed.; Wiley & Sons: New York, 1983; Chapter 4.
59. Shetty, D. K.; Rosenfield, A. R.; McGuire, P. Bansal, G. K.; Duckworth, W. H. Biaxial Flexure Tests for Ceramics. *J. Am. Ceram. Soc.* **1980**, *59* (12), 1193–1197.

Appendix. Hertzian Equations

Equation 1. Contact Radius (a)¹:

$$a = \left(\frac{4kPR}{3E} \right)^{1/3}, \quad (\text{A-1})$$

where

a = contact radius,

k = dimensionless constant,

P = indentation load,

R = sphere radius, and

E = Young's modulus of specimen.

Equation 2. Dimensionless constant (k)¹:

$$k = \frac{9}{16} \left[(1-\nu^2) + (1-\nu'^2) \frac{E}{E'} \right], \quad (\text{A-2})$$

where

ν = Poisson's ratio of specimen,

ν' = Poisson's ratio of sphere,

E = Young's modulus of specimen, and

E' = Young's modulus of sphere.

Equation 3. Mean contact stress (p_o)¹:

$$p_o = \frac{P}{\pi a^2}, \quad (\text{A-3})$$

where

p_o = mean contact stress.

¹Lawn, B. R. Indentation of Ceramics With Spheres: A Century After Hertz. *J. Am. Ceram. Soc.* **1998**, 81 (8), 1977–1994.

Equation 4. Tensile stress (σ_T)²:

$$\sigma_T = p_o \left(\frac{1-2\nu}{2} \right) \left(\frac{a}{\rho} \right)^2, \quad (\text{A-4})$$

where

σ_T = tensile stress at surface, and

ρ = radial distance along surface from center of contact.

²Lawn, B. R.; Wilshaw, R. Review Indentation Fracture: Principles and Applications. *J. Mater. Sci.* **1975**, *10*, 1049–1081.

NO. OF
COPIES ORGANIZATION

1 DEFENSE TECHNICAL
(PDF INFORMATION CTR
only) DTIC OCA
8725 JOHN J KINGMAN RD
STE 0944
FORT BELVOIR VA 22060-6218

1 DIRECTOR
US ARMY RESEARCH LAB
IMNE ALC HRR
2800 POWDER MILL RD
ADELPHI MD 20783-1197

1 DIRECTOR
US ARMY RESEARCH LAB
RDRL CIM L
2800 POWDER MILL RD
ADELPHI MD 20783-1197

1 DIRECTOR
US ARMY RESEARCH LAB
RDRL CIM P
2800 POWDER MILL RD
ADELPHI MD 20783-1197

1 DIRECTOR
US ARMY RESEARCH LAB
RDRL D
2800 POWDER MILL RD
ADELPHI MD 20783-1197

ABERDEEN PROVING GROUND

1 DIR USARL
RDRL CIM G (BLDG 4600)

NO. OF
COPIES ORGANIZATION

ABERDEEN PROVING GROUND

20 DIR USARL
 RDRL WM
 J MCCAULEY (10 CPS)
 RDRL WMP C
 T BJERKE (10 CPS)